Student thesis series INES nr 401

# Geometric quality assessment of multi-rotor unmanned aerial vehicle borne remote sensing products for precision agriculture

**Jayan Wijesingha**

2016
Department of
Physical Geography and Ecosystem Science
Lund University
Sölvegatan 12
S-223 62 Lund
Sweden

Jayan Wijesingha (2016).
***Geometric quality assessment of multi-rotor unmanned aerial vehicle borne remote sensing products for precision agriculture***
Master degree thesis, 30 credits in Master of *Geomatics*
Department of Physical Geography and Ecosystem Science, Lund University

Level: Master of Science (MSc)

Course duration: January 2016 until September 2016

**Disclaimer**

# Geometric quality assessment of multi-rotor unmanned aerial vehicle borne remote sensing products for precision agriculture

---

Jayan Wijesingha

Master Thesis, 30 credits, in *Geomatics*

**Supervisor**: Lars Eklundh
Department of Physical Geography and Ecosystem Science
Lund University, Sweden

**Exam Committee**:
Veiko Lehsten, Department of Physical Geography and Ecosystem Science
Lund University, Sweden
Per-Ola Olsson, Department of Physical Geography and Ecosystem Science
Lund University, Sweden

# Abstract

Sub-meter level spatial resolution remote sensing products are essential for Precision Agriculture (PA) applications. Recent development of Unmanned Aerial Vehicle (UAV) with imaging sensors provides opportunity to generate sub-meter level, timely, and cloud free remote sensing products. This study is a preliminarily assessment of a multi-rotor UAV with consumer grade optical camera and five spectral band multispectral camera for PA applications especially in geometric aspect. The UAV was flown over the agriculture area and images from both cameras were acquired and Digital Surface Models (DSM) and Ortho-Mosaics were derived from the collected image data. Geometric and visual quality of the derived products were assessed and limitations were identified regarding to PA applications. The optical camera images derived 2.1 cm spatial resolution ortho-mosaic while multispectral ortho-mosaic from the UAV multipsectral images gave 5.6 cm spatial resolution. The horizontal geometric accuracies of the optical camera product and multispectral camera product were 2 pixels and less than one pixel respectively. Relative average elevation difference of agriculture crop area and non-crop area were 0.27 m and 0.14 m in derived DSM from optical images and multispectral images respectively. Blurriness of the UAV-borne images was identified as a limitation of the UAV remote sensing exercise and UAV motion blur, cloud shadow, and wind were noted as possible causes for the blurriness in this study.

**Keywords** : UAV, Precision Agriculture (PA), Geometric Accuracy, Blurriness, Ortho-Mosaic, Digital Surface Model (DSM)

# Dedication

This thesis work is dedicated to my mother and father, who have been a constant source of support and encouragement during the my whole life time. I am truly grateful for having you in my life. This work is also dedicated to my fiance, Anuradha Hettiarachchi, who have always loved me and pushed me to work hard.

# Acknowledgements

This thesis became a reality with the kind support and help of the many individuals and I would like to extend my sincere gratitude to all of them.

First, I would like to thank my thesis supervisor Prof. Lars Eklundh of the Department of Physical Geography and Ecosystems Science at Lund University. He always give his full cooperation to succeed this research work. Under his mentorship I have gained so much knowledge and experience. I am grateful for his guidance and generosity. I would also like to thank to the UAV team who is Research Engineer Marcin Jackowicz-Korczynski and Researcher Dr. Per-Ola Olsson who provided immense help during field activities.

I would like to express my special gratitude to my best friend in Lund, Stefanos Georganos who encouraged me and did the proof reading of the thesis. And I must say thanks to Abdalla Eltayeb and Christos Bountzouklis who always be with me as good friends in the hard times.

I am highly indebted to the Swedish Institute (SI) for granting me a full study scholarship to study at the Lund University. Without that financial support the whole two years of my studies might be a dream.

I want to thank to my parents, two brothers and my fiance in Sri Lanka who have loved and helped me unconditionally not only the thesis time but also through out my life.

I would thank to Hans Dufourmont and the Copernicus Land Monitoring Service team at European Environment Agency in Copenhagen for giving me opportunity to work on my thesis while I am employed.

Last not least, my thanks and appreciation also go to my colleagues, friends and staff at the department and people who have willingly helped me.

# Contents

# List of Abbreviations

| Abbreviation | Explanation |
|---|---|
| 3D | Three Dimension |
| AGL | Above Ground Level |
| BI | Blurry Index |
| CDL | Communication Data Link |
| ChP | Check Point |
| CMVS | Clustering Multi-View Stereo |
| CP | Control Point |
| DEM | Digital Elevation Model |
| DN | Digital Number |
| DSM | Digital Surface Model |
| DTM | Digital Terrain Model |
| GCP | Ground Control Point |
| GCS | Ground Control System |
| GLONASS | Globalnaya Navigazionnaya Sputnikovaya Sistema |
| GNSS | Global Navigation Satellite System |
| GPS | Global Positioning System |
| GSD | Ground Sample Distance |
| MSL | Mean Sea Level |
| MVS | Multi-View Stereo |
| NIR | Near Infrared |
| PA | Precision Agriculture |
| PMVS | Patch-based Multi-View Stereo |
| PSIQ | PhotoScan Image Quality |
| PV | Precision Viticulture |
| RGB | Red, Green, Blue |
| RMSE | Root Mean Square Error |
| RS | Remote Sensing |
| SFM | Structure From Motion |
| SIFT | Scale-Invariant Feature Transform |
| SNR | Signal-to-noise-ratio |
| TIN | Triangular Irregular Network |
| UAV | Unmanned Aearial Vehicle |
| UgCS | Universal Ground Control System |
| $W_{kw}$ | Weighted Average of the image quality assessment index |

# List of Tables

# List of Figures

# Chapter 1

# Introduction

## 1.1 Background

Remote Sensing (RS) provides efficient technology in order to examine and understand the phenology and other spatiotemporal characteristics of vegetated areas (Xie *et al.* 2008). Satellite RS plays a leading role in vegetation mapping, especially in forest mapping, wetland monitoring, land cover classification, and change detection. The mapping of agricultural areas and the monitoring croplands is a broad field with many applications that go under vegetation monitoring. Tasks like croplands mapping, the extraction of phenological variables, as well as yield forecasting are some of the most prominent satellite RS applications in the context of agricultural monitoring. However, weather conditions, cloud cover, limited spatial and temporal resolution of the satellite sensors as well as the limited public availability of the data may limit the efficiency of crop mapping using satellite RS.

Aerial photography and mapping which is a branch of RS, overcomes difficulties in satellite RS up to a certain level. It enhances the spatial and temporal resolution of the data and avoids the cloud problem. However, conventional aerial photography requires a manned aircraft and other equipment which makes it an expensive technique. A benefit over cost analysis reveals, that aerial photography is not an efficient method for agriculture monitoring and mapping (Candiago *et al.* 2015).

In the past decades, rapid technological advances have led to a reduction in the size of most electronic devices such as computers, phones, cameras, etc. Consequently, many doors have been opened related to remote sensing applications. Unmanned Aerial Vehicles (UAV) armed with small spectral, thermal or laser sensors and a Global Navigation Satellite System (GNSS) receiver promote high resolution RS applications in all aspects. UAV based RS has amplified agriculture crop monitoring and mapping due to the high spatial and temporal resolution as well as having low operational cost comparing to satel-

lite RS and manned aircraft mapping (Matese *et al.* 2015). UAVs are small aerial vehicles which can carry payload without being manned and which can be controlled from the ground and aim to transcend most of the limitations of satellite RS as mentioned previously. These vehicles implemented new opportunities in RS and photogrammetry.

Advantages of UAV RS includes a) low altitude flights, b) attaining images of the objects under examination from a shorter distance, c) acquisition of data in cloudy, dizzily weather, d) not as expensive as other remote sensing methods, and e) allowing real time image and video data collection (Ma *et al.* 2013). According to a review article, the first UAV remote sensing papers were published in the Istanbul ISPRS conference, in 2004 and at present there is a biennial conference for UAV since 2011 (Colomina & Molina 2014). This reveals how UAV applications are gaining popularity and importance in the field of remote sensing.

The review article by Salamı *et al.* (2014) mentions that, there are three categories of vegetation RS using UAV. The first category is passive vegetation RS which means there is no direct action after the product creation from UAV RS. Canopy cover mapping and species mapping are some examples for this category. Applications such as water stress mapping, plant health monitoring, weed mapping, and pathogen detection fall under the second category which is proactive vegetation RS. The products from this category are used to make decisions and often execute appropriate actions. Agriculture crop mapping and monitoring under proactive category is considered as Precision Agriculture (PA) (Candiago *et al.* 2015). The third vegetation RS category is the reactive category which is still under development and expected to blossom in the near future. The data collected from UAV RS are often used at same time to make decisions and execute actions. At present, the PA with UAV RS is the most prominent application.

PA introduces a new level of farming strategies to use resources efficiently by the precise identification of required resources. It can increase the farm production while at the same time reducing its cost. Irrigation and fertiliser management as well as weed and pathogen detection are some of the actions that can be taken easily due to the PA applications. More than 60% of UAV RS research applications have been used for PA (Salamı *et al.* 2014). PA of vineyards is the most common UAV RS application in comparison to other agricultural crop management (Matese *et al.* 2015). Other than that, olive, citrus, and peach like fruit crops have been mapped and monitored with UAV RS. Additionally, cereals (wheat, barley, rice) are major PA applications with UAV RS due to the relative ease of the operations and lower heterogeneity (Salamı *et al.* 2014).

However, UAV RS has some limitations due to platform reliability, sensor capability, and image processing techniques (Zhang & Kovacs 2012). The UAV flight plans include calibrations regarding flying altitude, speed, coverage and image overlap. During early

stages, UAVs were flown in 180 - 270 m Above Ground Level (AGL) (Laliberte *et al.* 2010).In later studies, UAVs were flown at 80 – 120 m AGL for collecting data for crop management and forest structure mapping applications. The UAV flying speed depends on the wind and overlapping of the images. According to recent studies, the average flying speed of UAVs is about $3ms^{-1}$ to $6ms^{-1}$ (Mesas-Carrascosa *et al.* 2014; Dandois *et al.* 2015). Most studies recommend an image forward overlap of 80-90% and side overlap of 50-60% (Mesas-Carrascosa *et al.* 2014; Dandois *et al.* 2015; Mathews 2015). However, all the data acquisition parameters are dependent on the UAV, the payload attributes, the nature of the application, and the image processing method.

## 1.2 Research Questions and Aims

PA is the most dominant UAV RS application at present and its demand is increasing rapidly. Most of the PA research work that has been published recently used UAV RS. The UAV platform, payload sensor, flight mission, and both geometric and radiometric quality assessment play a vital role in UAV RS PA applications.

The identified parameters which are common to most UAV RS applications are the overlap percentage and the appropriate time of the day to perform the flight mission. However, other calibrations such as geometric and radiometric assessment, flying height parameters and flying speed are dependent on the application (Primicerio *et al.* 2012; Matese *et al.* 2015; Candiago *et al.* 2015; Mathews 2015; Torres-Sánchez *et al.* 2013). Additionally, the final product information quality is an important facet of PA from UAV RS.

The main aim of this research is to provide an overview on UAV RS for agricultural crop mapping and monitoring applications focusing mainly in the appropriate flight and payload calibrations for a PA. This research is going to address how to collect data relevant for PA using a multi-rotor UAV with RGB and multispectral cameras. Finally, this thesis aims to address a combination of UAV and sensor payloads for PA in order to overcome limitations for further improving PA applications. Thus, this study will try to tackle the aforementioned related topics and shed some light on following objectives:

- Identify optimum configurations of the UAV for acquiring data for PA applications
- Obtain very high resolution products from UAV data for PA.
- Evaluate geometric and radiometric quality of the UAV RS products.
- Identify limitations and advantageous of the UAV RS product for PA applications.

# Chapter 2

# Literature Review

In this chapter, UAV related literature is presented with studies that focus on UAV RS precision agriculture applications.

## 2.1 Unmanned Aerial Vehicles (UAVs)

UAV is one of the terms used to define the Unmanned Aerial System (UAS) which has additional names such as Remotely Piloted Vehicle (RPV), Remotely Operated Aircraft (ROA), Remotely Piloted Aircraft (RPA) and Drone (Eisenbeiss 2009). UAS can be classified according to the takeoff and landing method, which are split in horizontal takeoff and landing and vertical takeoff and landing. Fixed-wing UAS (airplanes) and rotary-wing UAS (helicopter) are categorized under horizontal takeoff and landing (Tang & Shao 2015). UAS consists of three main parts, i) the Unmanned Aircraft (UA), ii) the Ground Control System (GCS) and iii) the Communication Data Link (CDL) (Colomina & Molina 2014).

UA is usually a fixed-wing or rotary-wing aircraft that has less than 30 kg minimum takeoff weight with payload. The payload consists of remote sensing, navigation and orientations sensors. The portable hardware and software system that is used to control and monitor the UA is called GCS. The signal system which communicates with the GCS and UA is defined as CDL (Colomina & Molina 2014).

The sensor system in the UAV payload should be matched with the takeoff weight limit of the system. Only 20% - 30% of the total weight can be allowed for sensor payload in the UAV system (Zhang & Kovacs 2012). Additionally, not only the weight but also the volume and power consumption of the sensor must be considered for the UAV sensor payload next to the application condition (Colomina & Molina 2014).

Recently, light weight, high resolution imaging remote sensing payloads have been developed. They can be categorised as i) optical cameras (consumer grade non metric

camera), ii) near infrared (NIR) and multispectral sensors, iii) hyperspectral sensors, iv) thermal cameras and v) laser scanners (Everaerts 2008; Colomina & Molina 2014). Navigation systems in UAS transmit data about aircrafts position, velocity and altitude in every given period while orientation systems provide the aircraft's orientation data which are raw, pitch and heading (Colomina & Molina 2014).

The UAV flight session delivers large amount of images which cover the study area. The acquired images do not have similar geometric or radiometric features due to the low altitude of the flight, display unstable camera position, various viewing angels, and camera motions (e.g forward), etc. Hence, traditional airborne photogrammetry or remote sensing techniques are difficult to apply in UAV captured images (Everaerts 2008). The latest developed technologies in computer vision have contributed to the advancement of an innovative method to process UAV images, namely, Structure-From-Motion (SFM) and Multi-View Stereo (MVS). These are novel techniques which are frequently applied to process UAV images and create 3D surface and ortho-photos (Nesbit 2014).

## 2.2 UAV-borne image processing

Both analogue and digital stereo photogrammetry processes involve overlapped aerial photographs with camera calibration parameters, fiducial marks, and high accurate surveyed 3-dimension (3D) Ground Control Points (GCP) (Nissen *et al.* 2014). In comparison to the photogrammetry technique, SFM does not need the above requirements. SFM processes multiple overlapping images using automatically extracted points with an iterative bundle adjustment (Snavely 2011). The SFM approach is best suited for multiple overlapping image sets from wide array sensors or images from a moving sensor (Westoby *et al.* 2012). The simultaneous estimation of the 3D structure of the scene and calculating the motion of the sensor is the principal of the SFM (Wei *et al.* 2013).

According to the reviews, SFM emerged in the 1990s in the computer vision community by the growth of automatic feature-matching algorithms. It has been expanded by new algorithms of feature detection, relative orientation, bundle adjustment, and MVS (Westoby *et al.* 2012; Nesbit 2014). The procedure of SFM for creating 3D scenes from multiple images can be divided into four steps and it is presented in Figure 2.1.

The first step of the procedure is to identify features (3D locations) and match the corresponding features in multiple images, captured from different viewing angles. Scale-Invariant Feature Transform (SIFT) algorithm is the key algorithm to detect features and match corresponding features in the SFM process (Westoby *et al.* 2012; Nesbit 2014; Snavely 2011; Nissen *et al.* 2014). The identification of key-points (or interest points) based on local pixel variances of the images is the initial step in SIFT. Next, key-points

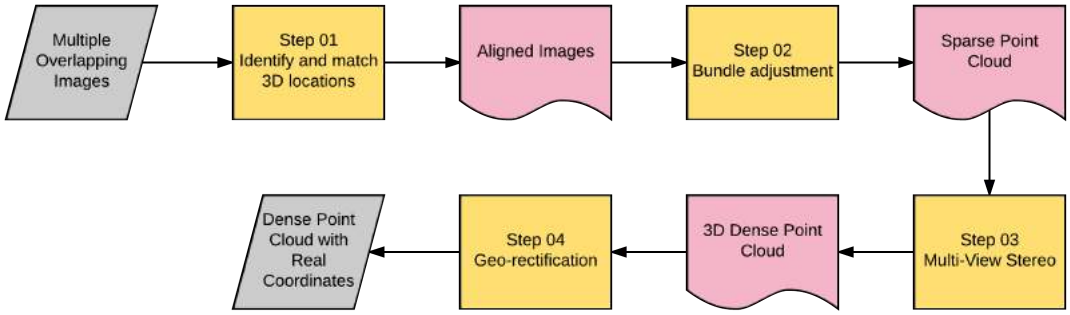


Figure 2.1: Basic steps in the SFM

are automatically matched to imprecise nearest neighbour in overlapping images. In that way, simultaneously outliers and improper matches are eliminated (Nesbit 2014).

Bundle adjustment is the second major step of the SFM and it is referred as 3D scene reconstruction (Westoby *et al.* 2012; Nesbit 2014; Nissen *et al.* 2014). In this stage, each camera position, orientation, camera parameters, and relative position of the corresponding features are calculated by using matching points in two or more photographs (Nissen *et al.* 2014; Westoby *et al.* 2012). The output of the bundle adjustment is a sparse point cloud. The sparse point cloud is a set of matching image data points in a three-dimensional coordinate system. The third step is MVS which derives a dense point cloud and 3D surface using known camera locations and SFM points (Westoby *et al.* 2012). The dense point cloud contains all the corresponding 3D points from the image set. An integrated Patch-based MVS (PMVS) algorithm and Clustering MVS (CMVS) algorithm are applied in this stage (Nesbit 2014). The CMVS clusters the point cloud while PMVS reconstructs a scene visible in the image set (Furukawa & Ponce 2010).

The last stage of the SFM process is geo-rectification which converts the dense 3D point cloud to a real geographic coordinate system (Westoby *et al.* 2012). Known camera position and focal lengths can be used for geo-rectification which is considered as a direct geo-rectification method without any external data. Pre surveyed Ground Control Points (GCPs) as external data are employed to geo-rectification, which is referred to as an indirect geo-rectification technique in SFM (Westoby *et al.* 2012; Nissen *et al.* 2014).

The SFM process was built in various open source and commercial software as one or a collection of separate packages (Nesbit 2014). One of the most prominent software based on the SFM is, Microsoft® Photosynth™ which develops 3D scenes for virtual tourism from crowd-source images (Snavely 2011; Westoby *et al.* 2012; Nesbit 2014). Bundler, CMVS and PMVS2 are stand-alone open source SFM software applications which apply different steps in the SFM process (Nesbit 2014). Integrated open source software packages using Bundler, CMVS and PMVS2 were created for SFM which are

SFMToolkit and VisualSFM (Westoby *et al.* 2012; Nesbit 2014).

Integrated SFM commercial software packages are Pix4D, Agisoft PhotoScan, EnsoMOSAIC, and Smart3DCapture (Nesbit 2014). In contrast to open-source packages, these commercial packages have a graphical user interface, continuous algorithm development and optimisation, customer support, and high accuracy georeferenced 3D outputs (Nesbit 2014). Both Pix4D and PhotoScan do not provide information on the exact SFM processing algorithms which are hidden in the packages.

According to forum discussion by Semyonov (2011) , PhotoScan has four major steps that are similar to the original SFM process. They are i) matching features, ii) solving camera and orientation parameters, iii) reconstructing dense surface, and iv) mapping texture using photo textures. Three main steps are used in the Pix4D software: i) extraction of key-points, matching key-points and optimisation of the camera model, ii) densification and filtering of points, and iii) generating a dense point cloud and Digital Surface Model (DSM) (Pix4D 2013). In the comparison of the two software systems, i) both provide efficient solutions for UAV mapping with high accuracy output of DSM and ortho rectified mosaic, ii) PhotoScan is more economical than Pix4D (academic institute licence price is about 549 USD and 1470 USD for PhotoScan and Pix4D, respectively as of 1st February, 2016). A comparative study of the two packages concluded that, both PhotoScan and Pix4D produce statistically similar geometrically accurate output but PhotScan is more user friendly than Pix4D (Gross 2015).

## 2.3 UAV RS data acquisition for PA

Studies related to data collection from UAV flights are limited due to the recent rapid development of the field. Usually, UAV follows a special flight plan with patterns of parallel lines which are called transects (Greenwood 2015). Each transect in the flight path is defined by way-points which guide UAV to fly according to the plan.

UAV image processing needs to meet similar image overlap criteria as in photogrammetry. Two image overlaps are considered: forward overlap and side overlap. The forward overlap is the percentage of one image cover from its previous or next image to the UAV flying direction. Side or lateral overlap is the percentage of one image cover from its parallel line image to the perpendicular direction of the flight path (Greenwood 2015). The UAV vertical position can be described using flying height or altitude. Flying height is the vertical distance from the Above Ground Level (AGL). Altitude is vertical distance from Mean Sea Level (MSL) (L'hotellier 2015). The flight plan includes flight path, how often images are taken, coverage of the one image, and total number of images to be taken. It is designed according to the inputs of the area to be mapped, operational

altitude, the amount of image overlap, and sensor type (Greenwood 2015).

UAV RS provides opportunity to change the Ground Sample Distance (GSD) of the products by changing flying height of the UAV. The GSD defines the ground distance between centres of the two adjacent pixels in the image (Pix4D 2013). The GSD of the image is dependeding on the UAV flying height, the width of the sensor, and the focal length of the sensor. Since, the sensor parameters are constant in the UAV RS, the flying height affects to the GSD directly. The lower the flying height, the lower the GSD of the image. However, lower flying height reduces the coverage of one image as well as total coverage of the flight mission. Therefore, flying height is a crucial parameter in the UAV RS PA exercises. Candiago *et al.* (2015) selected two different flying heights (100 m, 80 m) to map two different crops (grapes, tomatoes) to get the optimum quality output. However, constant flying height is not suitable for highly undulated terrain (Laliberte *et al.* 2010).

The flying method of the UAV is another important parameter in the UAV RS. Stop mode and cursor mode are the most common flying methods while images are being taken (Mesas-Carrascosa *et al.* 2014). The UAV stops when the image is being taken in stop mode but in cursor mode the UAV moves at the same speed while the image is being taken. Additionally, the turning method also a crucial flying parameter. Bank turn, Adaptive bank turn, and Stop and turn methods are the turning methods in the UAV mission. The UAV stops then turns in the Stop and turn method. The UAV keep the same speed when turning in the Bank turn method while the UAV slow down when turning in the Adaptive bank turn method (DJI-Innovations 2015). The turning method and the flying method are also dependent on the PA task. The study by Mesas-Carrascosa *et al.* (2014) recommended, 60m flying height and cursing mode to achieve the highest spatial and spectral resolution for forest mapping using UAV RS.

Weather condition also plays an important role in the UAV RS data acquisition. Sunny days creates clear light conditions and it increases the contrast of the images. However, shadow effects are higher in the sunny days comparing to cloudy days. To reduce the shadow effects data collection is done at high solar angles time such as noon or near to noon times (Dandois *et al.* 2015). Radiometric quality of the low altitude images are changed due to weather condition at observation (Kedzierski & Wierzbicki 2015). According to Kedzierski & Wierzbicki (2015) , the radiometric quality of the images which have been taken at various weather and light condition can be assessed using an index called Weighted average of the image quality assessment index ($W_{kw}$). The index can be computed using Equation 2.1.

$$W_{kw} = \frac{\sum_{i=1}^{n} W_i \left(\frac{\mu_i}{\sigma_i}\right)}{\sum_{i=1}^{n} W_i} \tag{2.1}$$

Where:

$W_{kw}$ is the weighted average of the image quality assessment index

$\mu_i$ is the mean pixel intensity value of the given $i^{th}$ band

$\sigma_i$ is the SD of the pixel intensity values of the given $i^{th}$ band

$W_i$ is the weight for the $i^{th}$ band determined from empirically base on luminance value

$i$ is the band number

$n$ is the number of bands in one image, (Kedzierski & Wierzbicki 2015)

The index was developed for RGB images and weights for each band in the RGB image is defined from luminance value equation. According to that, the weights for each band are $W_R = 0.299$, $W_G = 0.587$, and $W_B = 0.114$ (Kedzierski & Wierzbicki 2015). The index values between 1.1 to 2.7 define a good radiometric quality in the image while values more than 6.8 denote images of very poor radiometric quality. Images with index values between 2.7 - 5.6 and 5.6 - 6.8 are considered as medium radiometric quality and poor radiometric quality images respectively (Kedzierski & Wierzbicki 2015).

Image blurriness is another factor to be considered in UAV RS. It can be caused by the instability of the UAV due to during the flight and the sensor focusing issues, as well as vegetation movement due to the wind. Identification of blurred or non focused images before processing is very important in UAV remote sensing. In image processing context, there is number of advanced techniques to identify the blur level of the image and to extract the blurry area. The Agisoft PhotoScan provides an image quality estimation which is related to the image blurriness. The PhotoScan image quality value provides information about the sharp borders of the image (Pasumansky 2014). Nevertheless, no proper and detailed description has been provided about the algorithm of the image quality estimation in the PhotoScan. According to the Agisoft LLC (2016) user guide, images with a quality value below 0.5 are considered as blurry images. The value 0.5 is the minimum threshold value that recommend in the user guide. Finally, detecting blurriness of the UAV captured image is increasing the quality of the final output of the UAV RS and accuracy of the PA application.

As a summary of the recent research studies, there was a unique parameter specification on each UAV RS for PA application. Primicerio *et al.* (2012) mapped vineyards with a rotary-craft UAV with 3 band (G, R, NIR) multispectral sensor in Empoli, Italy. The flying height of the study was 150 m while the flight was execute at noon. The study by Matese *et al.* (2015) compared RS platform effects for PA in Italian vineyards. The vehi-

cle used in that study was a rotary-wing aircraft with a 3 band (G, R, NIR) multispectral sensor. Similarly, to the previous study, the flying height was set at 150 m while the flying speed was 4 $ms^{-1}$. Additionally, 72% forward overlap and 40% side overlap were selected in the flight plan of that study. PA over vineyard and tomato fields in Ravenna, Italy was performed by Candiago *et al.* (2015) . A multi-rotor aircraft with a 3 band (G, R, NIR) multispectral sensor was utilised in that study. Constant flying speed (3 $ms^{-1}$) and overlaps (forward and side - 75%) were maintained in both crop types. However, the flying height was different in the tomato fields (100 m) than vineyard (80 m). In comparison to the previously mentioned studies, geometric assessment was performed using 20×30 cm Ground Control Points (GCP). Moreover, Mathews (2015) engaged PA in vineyard monitoring in Texas, USA. A fixed-wing aircraft was used in that study with two consumer grade cameras with filters (RGB and NIR). The UAV was flown at 125 m height at noon. Geometric assessments was performed using 0.6×0.6 m GCP. Additionally, radiometric calibration was executed with help of colour targets and filed spectrometer data. The last reviewed study is different PA application which relates to weed management with UAV RS (Torres-Sánchez *et al.* 2013). A multi-rotor UAV with RGB optical camera and 6 band (B, G, R, RedEdge, NIR, master) multispectral camera were used in that study. Additionally, constant overlap coverage was maintained while the UAV was flown in three flying heights (30 m, 60 m, 100 m). Geometric assessment was performed with 1×1 m GCP. As a summary of the aforementioned applications, UAV RS were used for crop heterogeneity mapping, vegetation index calculation, agriculture crop and weed crop identification, soil and crop separation are prominent PA applications. However each application has a unique sensor and a unique way of acquiring images which depend on the application, the UAV and the sensor.

The UAV RS produces two main important outputs from the UAV-borne images processing. The first product is a Digital Surface Model (DSM) which represents elevation model of the top faces of all objects above the terrain (Jedlika 2009). The other product is an ortho-mosaic. The mosaic is a single image that generated by merging collection of adjacent images. Similarly, the ortho-mosaic is created by merging adjacent ortho-photos. The optimum UAV RS product specification and quality criteria for the PA applications are dependent with the application type. RS products with 20 cm - 50 cm spatial resolution are recommended to the Precession Viticulture (PV) application (Primicerio *et al.* 2012). Spatial resolution 4 cm and less than 100 m flying height were suggested by Torres-Sánchez *et al.* (2013) to identify weed plants from agriculture crops using UAV RS. Similarly, 5 cm spatial resolution and 3 pixel level geometrically accurate RS products from the UAV can be used to calculate volume of the sugar cane plant and weed management (Yudi *et al.* 2015). Thus, UAV RS product specification and the quality level

also depends with the UAV, the payload and the application type.

In reality, each UAV platform and each sensor payload have their own configurations and each PA application has its unique assessment method. Thus, it is necessary to perform additional studies that increases the fidelity in selection flying parameters for future PA applications.

## 2.4 Geometric accuracy assessment

Remote sensing products are usually evaluated for geometric accuracy to showcase how much they can be referred to the real world. The most common way to do so is through geo-referencing a remote sensing product or image (Greenwood 2015). Ground Control Points (GCP) are used to geo-reference images which have both real geographic coordinates and image coordinates. The distribution and number of GCPs change the geometric accuracy of the product. A GCP is a fixed mark or point on the ground which can be seen on the acquired images. The size of the GCP should be matched with the image spatial resolution and sensor type. A GNSS survey is carried out to assign 3D geographic coordinates for the GCP. The survey can be done before or after the UAV flying. Modern software of UAV image processing use camera location as a GCP and process images with geographic coordinates (Greenwood 2015).

The geometric accuracy can be evaluated by calculating an absolute accuracy and a relative accuracy. The absolute accuracy is the most common statistical assessment of random and systematic errors encountered in the horizontal or vertical position on the image with respect to the datum. It can be described by using a Root Mean Square Error (RMSE) value as shown in Equation 2.2 (Riazanoff & Santer 2006). The RMSE is an indicator of the absolute geometric accuracy of the RS product (Mesas-Carrascosa *et al.* 2014).

$$RMSE = \sqrt{\frac{1}{n}\sum_{i=1}^{n} dist\left[(\lambda_i, \varphi_i)\,(\Lambda_i, \Theta_i)\right]^2} \tag{2.2}$$

Where:

$n$ is the number of GCP

$(\lambda_i, \varphi_i)$ is the geographic location in the image point i after geo-referencing

$(\Lambda_i, \Theta_i)$ is the geographic location in the point i given by reference data

$dist$ is the distance function (euclidean distance or geodetic distance)

The distribution and number of GCPs play a vital role in the geometric accuracy assessment. Usually, 4 or 5 GCPs are utilised to geo-reference an ortho-mosaic. In most

studies they are located in four corners of the mapped area and the centre of the area (Mesas-Carrascosa *et al.* 2014; Mathews 2015). A study by Goldstein *et al.* (2015) showed, 10 GCPs provide the highest RMSE for the UAV mapping area which has 0.025 $km^2$ and more than 10 GCPs do not change the RMSE significantly. The aforementioned studies summarised, number of GCPs used in the geo-reference process and GCP distribution are important facts in the UAV RS.

## 2.5 Radiometric calibration

A sensor acquires the reflected energy from the object and records it as a brightness value which is called as a Digital Number (DN) in RS. The collected brightness values are depended on the weather, the light condition, the sensor, and data compression conditions. Therefore, the data collected from UAV RS need to be evaluated for the radiometric quality. "Detailed mapping of local irradiation changes recorded by the imaging system while maintaining a continuum of brightness adequate for the mapped scene" is the definition of the radiometric quality of the digital image (Kedzierski & Wierzbicki 2015).

Image contrast, random noise, and radiometric resolution indicate the internal radiometric quality of the image. Signal-to-noise-ratio (SNR) of the image, stability of the sensor, and radiometric accuracy describe the central radiometric quality of the image. Furthermore, sharpness, resolution and contrast of the image describe the radiometric image quality affected by the sensor (Kedzierski & Wierzbicki 2015).

Radiometric and spectral calibration are applied to improve the radiometric quality of the observed images from the sensors. Laboratory calibration, on-board calibration, and vicarious calibration are the radiometric calibration methods used in the field of remote sensing (Riazanoff & Santer 2006). Calibration using in-situ measurements collected on the field campaign refers to vicarious calibration. It enables the calibration of the collected data according to flight conditions (Del Pozo *et al.* 2014). Additionally, radiometric calibration includes conversion from DN values or radiance into reflectance. Reflectance is unrelated to lightning conditions and therefore the preferred unit of the final data. However, a precise computation requires very accurate calibration procedure. A relative calibration to a common standard (e.g. ground target) might be sufficient.

Most UAV RS studies used vicarious calibration for the radiometric calibration. Mathews (2015) used artificial targets with different colours (blue, green, red) to calibrate UAV RS product from multispectral sensor with 4 bands. Spectrometer reading and digital levels of the images of the spectral targets were analysed using linear regression model to identify the relationship between DN values and spectral reflectance of each band.

# Chapter 3

# Methodology

This chapter is dedicated to the presentation of the UAV and data acquisition and image processing. It describes the software and algorithms which were used in this study.

## 3.1 UAV and Payload

The UAV which was used in this study is a rotary-wing aircraft (quadcopter) which is called 'Explorian'. It was manufactured by Pitchup AB (Sweden). The aircraft is of a vertical take-off and landing type and equipped with 4 motors plus carbon rotors (30 cm). Both motors and payload are powered by a 24.0 V (22000 mA) battery. The UAV is 1 m wide, 1 m long with expand rotary and has a 40cm tall frame. The take-off and landing of the UAV needs to be done using a remote controller which has 500 m radius of control. The UAV can be flown manually or automatically with a pre-designed flight plan. All the electronic connections in the UAV are covered with a plastic lid to prevent interaction with rainwater. The average flying time of the Explorian with payload is 20 minutes. Figure 3.1 shows the UAV and during a flight.

The payload of the UAV includes an accelerometer, a gyroscope, a positioning system, a compass, an air telemetry module, a black box, and the RS payload. Both accelerometer and gyroscope are inertial sensors which measure acceleration and rotation of the aircraft. The positioning system consists of a Global Positioning System (GPS) receiver which helps navigation. The compass is a magnetometer which aids to find the facing direction of the UAV and it is very sensitive to magnetic interference. The telemetry module sends current position, altitude, and angles of the vehicle to the GCS and receives user commands through the flight controller. A black-box stores a log of the flight session which functions as a data-logger.

The Explorian's GCS includes a flight controller, a telemetry data viewer, and a GCS software. The flight controller communicates with the UAV through radio waves. The

(a) When the UAV is not moving (b) UAV during the flight session

Figure 3.1: The Explorian UAV

flight controller switches are associated with forward/backward (pitch) motion, elevation, clockwise or counter-clockwise rotation (yaw), roll, gimbal control, flight mode, and return mode. Two main controllers are needed to start the engine of the UAV. The flight controller has a separate telemetry data viewer which shows telemetry data of the flight and is connected with the sensor live video. The telemetry data contain flying height, flying speed, current location, rotation parameters, and battery level.

The GCS software is called UgCS which abbreviates as Universal Ground Control Software. It is a flight control software from SPH Engineering in Riga, Latvia which has both free and commercial versions and can be customised to different UAVs. The screen view of the UgCS is illustrated in Figure 3.2. The UgCS provides the capability to plan missions, view old flight sessions & geo-tag photos, control sensing payloads, switch flight mode, and receive & view telemetry data.

### 3.1.1 Remote Sensing Payload

The remote sensing payload in the Explorian UAV includes a visible camera, a multispectral camera, and a thermal camera which can be triggered automatically according to the user configurations. RGB and multispectral cameras in the Explorian UAV are shown in Figure 3.3. The thermal was not used in this study due to a technical failure.

The visible camera in the system is a SONY A6000 (ILCE-6000L) Digital Single-Lens Reflex (DSLR) camera which is powered by its own rechargeable battery. It is equipped with a 24.3 mega-pixel Advanced Photo System (APS) Type-C (Classic) Complementary Metal-Oxide-Semiconductor (CMOS) sensor (23.5$\times$15.6 mm). The sensor has an ISO range between 100-25600. The camera records 8-bit data in JPEG and RAW formats which have a size of 4000 x 6000 pixels. The lens in the camera range between 16-50 mm power zoom with 83°- 32° angle of view (Sony 2011). The RGB camera is

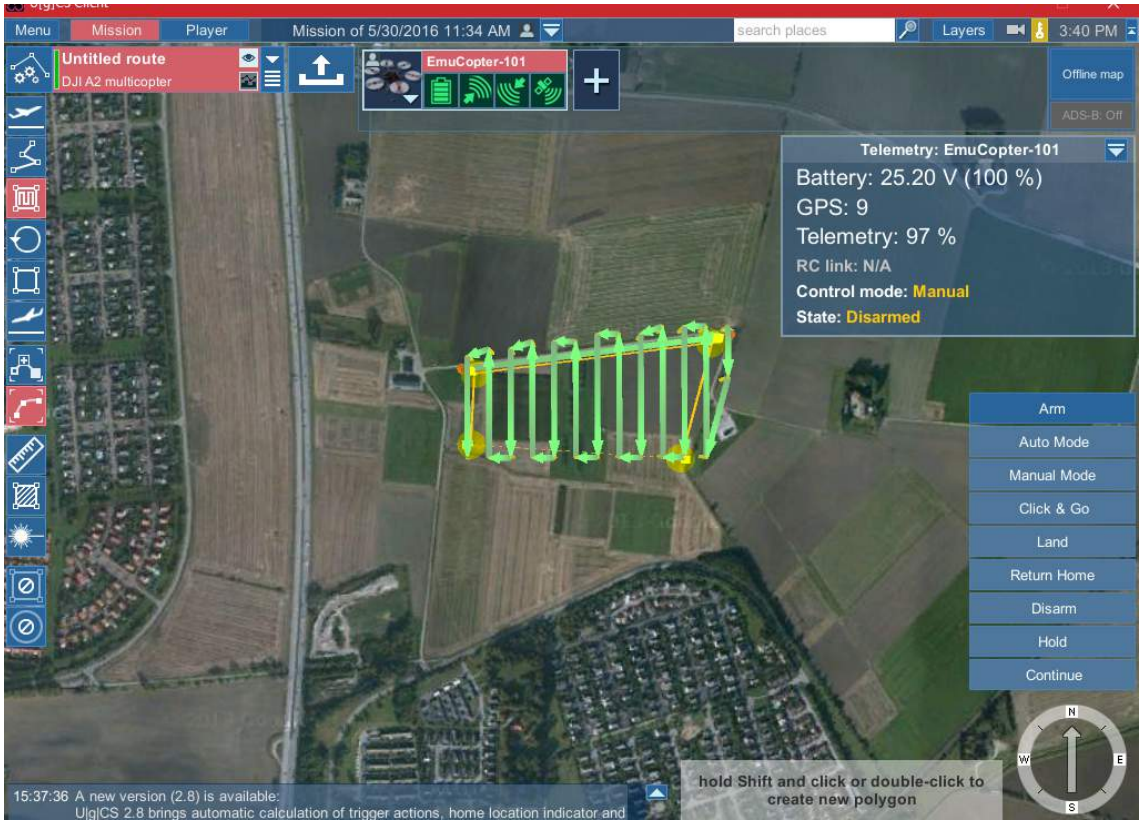


Figure 3.2: The UgCS Software

mounted to the UAV with a gimbal that helps to keep constant viewing angle of the camera and to provide near-nadir images.

The multispectral instrument in the payload is a Micasense RedEdge™ multispectral camera. It is a low-weight sensor specially designed for UAV mapping. It has dimensions of 12.1 cm×6.6 cm×4.6 cm. It includes 5 spectral filtered cameras which provide 5 spectral bands Blue, Green, Red, Red Edge, and Near Infrared simultaneously in one capture. Spectral information of the bands are presented in Table 3.1. The GSD of the sensor is 8.2 cm/pixel when at 120 m AGL and Horizontal Field of View (HFOV) is 47.2°. The sensor is powered by the UAV battery and it needs 5.0 V Direct Direct Current (DC) (Micasense 2015). The RedEdge sensor can be configured through the WiFi connection and it has its own inbuilt WiFi modem. The user can trigger the camera, design the flight mission (overlap, flying height), and configure other settings via the WiFi connection. The RedEdge camera captures images as RAW Digital Negativ (DNG) (12-bits) or RAW TIFF (16-bits) while the resolution of the image is 1280×960 pixels. The multispectral sensor has its own positioning system which aids to geo-tag captured images.

Table 3.1: Spectral bands in the RedEdge Multispectral Sensor (Micasense 2015)

| Band No | Band Name | Center Wavelength (nm) | Bandwidth (nm) |
|---|---|---|---|
| 1 | Blue | 475 | 20 |
| 2 | Green | 560 | 20 |
| 3 | Red | 668 | 10 |
| 4 | Near IR | 840 | 40 |
| 5 | Red Edge | 717 | 10 |


(a) Sony A6000 RGB Camera (Sony 2011)


(b) Micasense RedEdge Camera (Micasense 2015)

Figure 3.3: Remote Sensing Payload in the UAV

## 3.2 Study Area

UAV flight sessions were performed at the Lönnstrop research agriculture field which is located in between Lund and Lomma in southern Sweden. Centre coordinates of the area are 55.669395°N and 13.106488°E. It is about 500 m x 200 m in size and includes several types of crops (beats, barley, wheat).

## 3.3 UAV Data Collection

### 3.3.1 UAV flight mission

The UAV flight missions were designed using the mission planner software UgCS. The route design was based on the RGB camera configuration. The GSD of the capturing images was set as 2 cm and overlap of the images were set as 80% and 60% for forward overlap and side overlap respectively. The flying speed of the UAV was adjusted to 5 $ms^{-1}$ and 'Adaptive Bank Turn' was chosen as the turning method of the UAV. The flight path was computed using the aforementioned parameters. The designed flight path was uploaded to the UAV before the mission was executed.

The RedEdge camera was configured separately. Parameters of RedEdge camera flight mission are much similar to the RGB camera. In the configuration process, both overlaps were set to 80% and the flying height was set to 90 m. Additionally, all five bands of the camera were selected to capture images and writing image type was set as 16bit TIFF file. The configuration details were saved automatically in the camera at the end of the configuration process.

The flight mission and the RedEdge flight planning were checked and confirmed again just before the take-off of the UAV. A minimum of three people are preferred to execute a flight mission safely. One person controls the remote flight controller, the second checks the live view and telemetry data, and the third person works with the UgCS and monitors the flight mission. However, it is possible to fly with fewer persons, but it is more tricky.

First, the Explorian UAV was manually taken-off using the controller up to the certain height (~20 m). After the UAV reached the required height, the flight mode was changed from manual to auto through the UgCS. Then it followed the uploaded flight path and the RGB and the RedEdge camera were triggered according to the configured settings. Live view and telemetry data were observed through the viewer. Simultaneously, the position of the UAV and log messages were monitored through the UgCS when during the mission.

Figure 3.4: During the UAV flight session

When the UAV finished the full flight path, it started to hover to the last waypoint. Then auto mode was changed to manual mode using the flight controller. Next, the UAV was landed using the controller to a nearby place from where it was taken off.

### 3.3.2 Ground Observation

Ground data collection is important for a successful UAV remote sensing project. GCP location observation and the RedEdge sensor calibration image were the components for

geometric and radiometric calibration in this study. Figure 3.5 shows steps in the ground observation.

Target plates (290 mm×290 mm) with white cross mark (Figure 3.5c) were used to locate the GCP. The target plates were distributed over the study area before the flight session was done. Real Time Kinematic (RTK) GPS+GLONASS observation was performed on the each GCP and position data was recorded. The horizontal and vertical accuracy of the point observations were 0.015 m and 0.030 m respectively. All the position data were collected under the SWEREF99 TM coordinate system and SWEN08-rh2000 geoid.

The Micasense RedEdge camera has its own white calibration panel for radiometric normalisation. Two photographs of the calibration panel were taken before and after the flight session in all five bands to perform radiometric calibration.

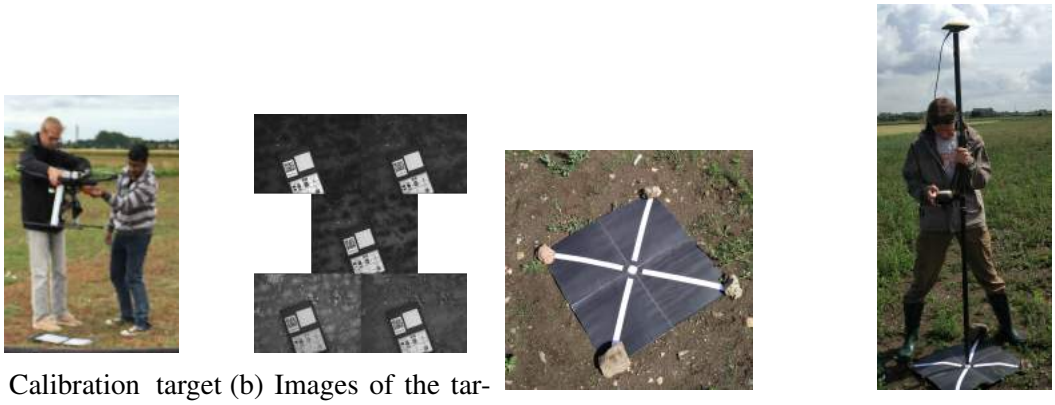

(a) Calibration target observation (b) Images of the target (c) GCP target plate (d) GNSS observation

Figure 3.5: Ground Observation Process

## 3.4 RGB Image Analysis

RGB images from the UAV flight sessions were analysed for the effect of weather and light conditions, effect of the image blurriness, and geometric quality with distribution of GCPs. A flow chart which describes each test is presented in Figure 3.6.

RGB image sets from two flight sessions (two dates) over same the study area were analysed for the light and weather condition effect on the acquired image quality. The $W_{kw}$ index for each image from both data sets were computed. The index values were compared and analysed with the weather and light condition of each day.

### 3.4.1 Test for RGB image - blurriness effect

The PhotoScan Image Quality Index (PSIQ) values for RGB images from the flight session over the study area were calculated. The values from the index were plotted against

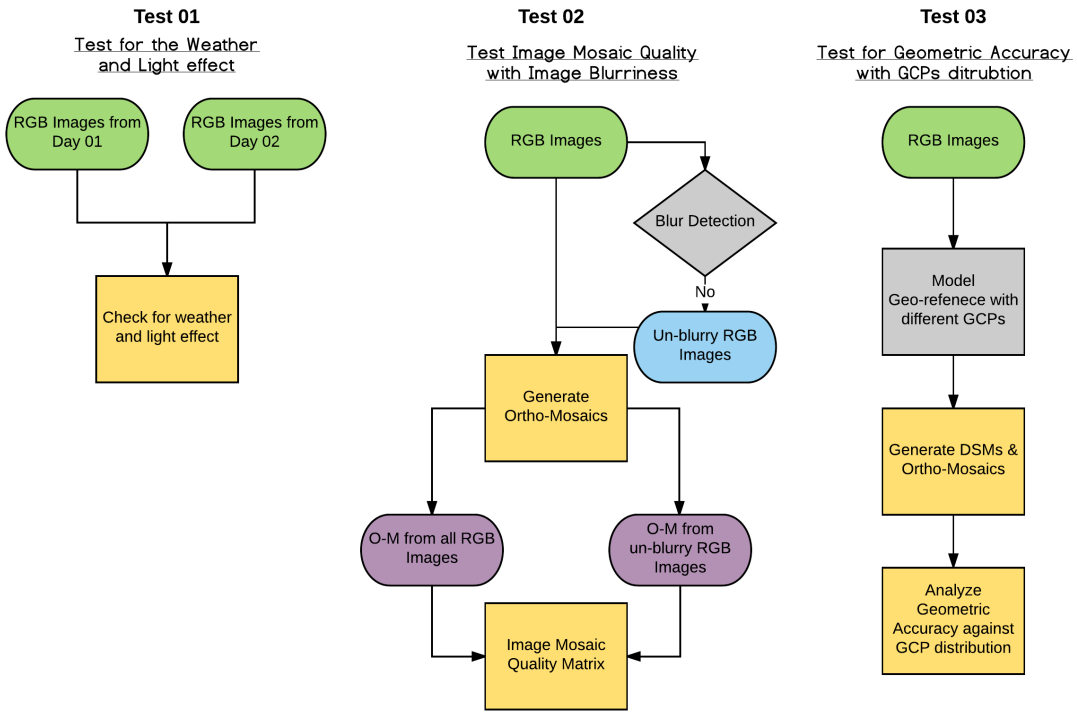


Figure 3.6: The flow chart of RGB image analysis

the image number and the distribution of the index values was studied to indicate the relationship between image blurriness and the UAV position. According to the PSIQ value distribution, the threshold value was defined as 0.65 to separate blurry from non-blurry photos. The threshold value was updated from 0.5 to 0.65 due to obtain more quality images. After, two RGB ortho-mosaics were generated using all the RGB photos and only using non-blurry photos respectively.

The Agisoft PhotoScan Professional Version 1.2.5 (64 bit) full trial version software was used for ortho-mosaic generation. Ortho-mosaic generation using UAV images with the PhotoScan is a step by step process and it is illustrated in Figure 3.7. First, images were aligned using matched point and geo-tag information of the photos. A point cloud with arbitrary coordinates were generated in this step. The point cloud was optimised and geo-referenced using external GCP data in the optimisation step. Next, the point cloud was processed to generate a dense point cloud which has all the matching points from the image set. Later, the dense point cloud was further processed to generate a mesh which is a Triangular Irregular Network (TIN) like point cloud (Mathews 2015). Then, the DSM was derived from the dense point cloud. The Digital Terrain Model (DTM) only contains elevation on the terrain (Jedlika 2009) and it could be derived from the DSM by using only ground points in the dense point cloud. Ortho-rectification and image mosaic creation is the final step of the process and it uses the generated point cloud and DSM or DTM that

generated in previous step.

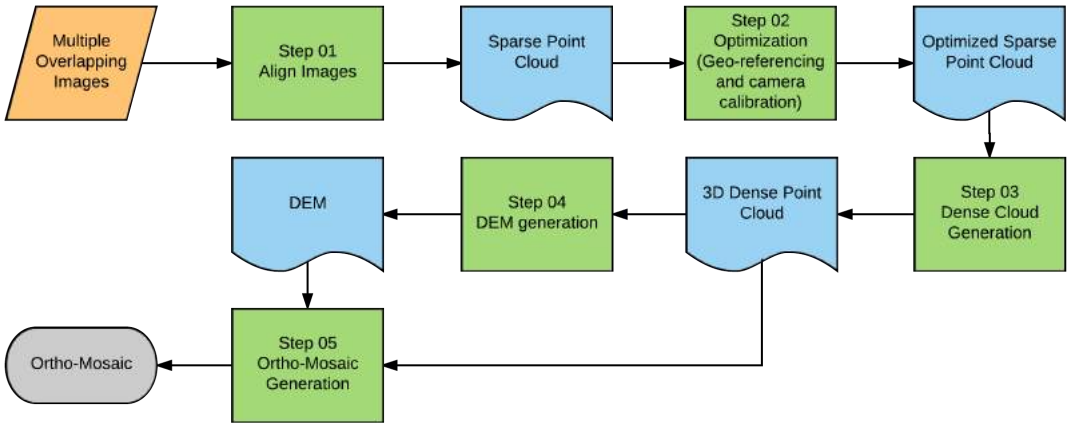


Figure 3.7: Ortho-Mosaic generation process in the Agisoft PhotoScan

Ortho-mosaics generated from all RGB images and non-blurry RGB images were visually compared. The blur level in the ortho-mosaic was quantified with algorithm suggested by Rosebrock (2015) : The ortho-mosaic was filtered with convolution filter with a Laplacian kernel and the variance of the filtered image was considered as quantification for the blurriness. The lower variance value indicates higher blurriness (Rosebrock 2015).

### 3.4.2 Test for RGB image - geometric accuracy

Table 3.2: CPs and ChPs distribution in the geometric analysis

| GCP Option | No. CP | No. ChP |
|---|---|---|
| P1 | 5 | 7 |
| P2 | 5 | 7 |
| P3 | 6 | 6 |
| P4 | 9 | 3 |

The effect of the number of GCPs and GCP distribution was examined in this section. RGB images acquired from one UAV flight session with 12 GCPs were used. Four ortho-mosaics were generated by changing GCP distributions using PhotoScan. In each occasion some GCP were used as Control Points (CP) and others were used as Check Points (ChP). The number of CPs and ChPs in each analysis option are tabulated in Table 3.2. RMSE value for each option was computed using check points and error and GCP distribution was examined.

## 3.5 Multispectral (RedEdge) Image Analysis

Multispectral images from the RedEdge camera were acquired from two UAV flight sessions in two days over the study area. Similar to the RGB image analysis, RedEdge camera images were analysed for different light condition by computing the $W_{kw}$ values from each image (Kedzierski & Wierzbicki 2015).

Similarly, blurriness analysis, was followed as in the RGB image process. The blur effect of the RedEdge camera image was analysed by computing the PhotoScan image quality values. Images which had quality index below 0.85 were removed from further processing. Likewise RGB image analysis, the threshold value was increased from the recommended value to reduce blurry images from the image set. The remaining images were utilised to generate a multispectral ortho-mosaic. The blue spectral band was always selected as a master channel to align spectral bands of the ortho-mosaic generation process in the PhotoScan.

The geometric quality analysis for the RedEdge camera images followed the same procedure as in the RGB images. The highest geometric quality multispectral ortho-mosaic was used to create maps of the study area. The radiometric calibration was not performed due to unavailability of incoming radiation data in the flight session.

Finally, ortho-mosaics from RGB images and multispectral images were visually compared and examined.

# Chapter 4

# Results

The outputs results from the study are described in this chapter.

## 4.1 UAV-borne Images

Two data collection flight sessions were performed on 01$^{st}$ July and 12$^{th}$ August over the study area. The two flight paths with GCPs are showed in Figure 4.1.The average flying height of both flight sessions was 95 m. The flight session on the first day, covered an area of 0.121 km$^2$ while the other flight session covered 0.073 km$^2$. Both flight sessions were performed near to the solar noon to avoid shadow effect.

In the first flying session, the RGB camera was set to trigger in every 12 meters on the flight route and total 132 images were expected. However, only 75 images were acquired in the flight session. Similar to the first day, in the second flight session 70 RGB images were supposed to be acquired. Nevertheless, only 48 images were captured from the flight session. All RGB images were taken with auto configuration of the camera. The RGB camera selected aperture size (1/f) and shutter speed according to light condition but, ISO was fixed to the lowest possible value (100).

The multispectral RedEdge camera does not provide any data about the number of images that will be taken in the flight session. However, it starts to capture images from the moment that the UAV starts to fly. When it acquires images, it always follows the settings (overlap, file type, etc.,) that is configured before the flight session. At one capture five separate images are recorded, one for each spectral band. In the first day flight session a total of 192 images were captured. Images only covering the study area were used for further processing (150 images). Similarly, 120 images were collected on the second day flight session but only 95 images were used. Overview of the flight sessions are presented in Table 4.1.


(a) The UAV flight path - Day 01


(b) The UAV flight path - Day 02

Figure 4.1: The UAV flight paths from both days

## 4.2 Weather and Light condition effect

On the first flight session the weather was cloudy and overcast comparative to the second day. There was not much sunlight on the both days due to heavy cloud cover. The recorded wind speed at flying time on the first day was about 6 $ms^{-1}$ and the second day it was about 5 $ms^{-1}$ (The Weather Company 2016).

According to the Weighted average of the image quality assessment index ($W_{kw}$) value criteria, 1% of good quality images and 21% of very poor quality images were categorised from the first day RGB image set. In contrast, 91% of RGB images from the day two had medium quality and there were no good or poor quality images. However there were very poor quality images which are 9% of the total images. The percentage of good or medium

Table 4.1: Summary of the flight sessions

| **Session** | Flight Session 01 | | Flight Session 02 | |
|---|---|---|---|---|
| **Date and Time** | 2016-07-01 10.00 AM | | 2016-08-12 10.30 AM | |
| **Weather** | Overcast, Windy | | Overcast, Windy | |
| **Camera** | RGB | RedEdge | RGB | RedEdge |
| **No of Images** | 75 | 150 | 48 | 95 |

quality images from the flight session was greater in the second day. Moreover, the first flight session delivered many very poor quality images due to light condition than the second flight session.

Table 4.2: The $W_{kw}$ index values for RGB and RedEdge images

| $W_{kw}$ **Quality Level** | **RGB - Day 1** | **RGB - Day 2** | **RE - Day 1** | **RE - Day 2** |
|---|---|---|---|---|
| Good | 1% | 0% | 23% | 9% |
| Medium | 65% | 91% | 56% | 77% |
| Poor | 13% | 0% | 13% | 3% |
| Very Poor | 21% | 9% | 7% | 10% |

Similarly, the RedEdge camera image set was categorised according to the $W_{kw}$ values. The $W_{kw}$ values for each image set are presented in Table 4.2. 23% and 9% of the total images were identified as good quality from the first and second day flight sessions respectively. In contrast, very poor quality images due to light condition were identified and they are 8% and 10% of the total images from both flight session respectively. Both days provided more medium quality images and they are 56% and 77% of the total images from day 01 and day 02 respectively. 13% and 3% of total images from each flight session were categorised as poor quality images. In the same way to the RGB image sets, the second flight session provided more better and medium quality RedEdge images than the first day flight session.

The $W_{kw}$ values from the RGB and RedEdge images show that the second flight session produced images of better quality in comparison to the first.

## 4.3 Blur effect

The PhotoScan Image Quality (PSIQ) values were calculated for both RGB and RedEdge camera image sets taken on the second flight mission. A threshold value to detect sharp images from the RGB image set was considered as 0.85 and from RedEdge images it was 0.65. The image locations and PSIQ values were mapped to check how flight path influenced the blurriness of the images. Two PSIQ location maps are shown in Figure 4.2. According to the maps, there is high risk of finding blurry images at turning curves

of the flight path than straight lines. In comparison, percentage of images being blurry is higher in the RedEdge image set than the RGB image set.

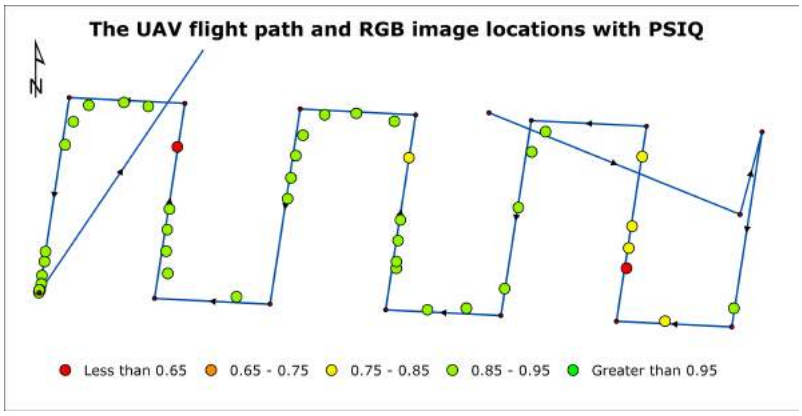


(a) RGB image locations and PSIQ

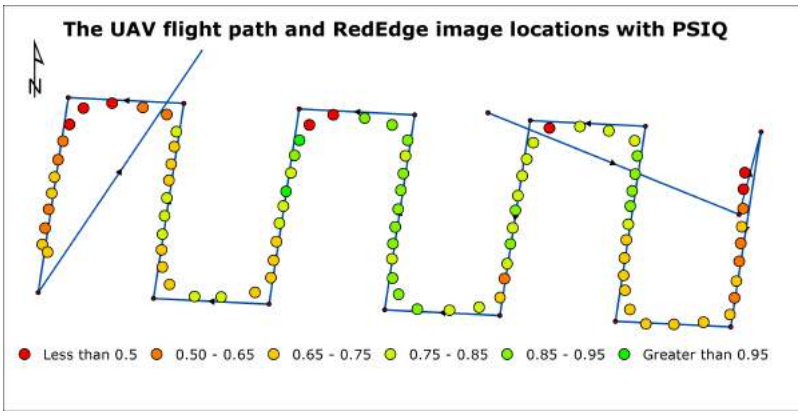


(b) RedEdge image locations and PSIQ

Figure 4.2: The UAV flight path and PSIQ values from the images

Seven images from the RGB image set were categorised as blurry from threshold value. Two ortho-mosaics were generated using all RGB images and non-blurry RGB images. In comparison, there is no significant visual changes on both ortho-mosaics. However, Rosebrock (2015) 's blurriness index (BI) values for both mosaics reveals that the mosaic only containing sharp images displays less blurriness than the other one. The mosaic with all images resulted in a BI value of 118.88 while the other mosaic which only contained sharp images got a BI value of 138.13. However, the higher the BI value the lower the blurriness of the image. Consequently, removing blurry images from the image processing reduced the effect of the blurriness of the output.

The blurriness analysis for the RedEdge image set was similar to the RGB image set. Likewise to the RGB images, two ortho-mosaics were created using all RedEdge images and images categorised as non-blurry. Two mosaics were analysed for blurriness using the BI values. The BI value of the mosaic with only sharp images was 120.70 and the BI value for the all image mosaic was 97.13.

Finally, both RGB and RedEdge images show, eliminating blurry images based on the PSIQ would reduce the total blurry effect from the final product.

## 4.4 Geometric Accuracy

The third test for the UAV images was the analysis of the geometric quality of the ortho-mosaics. The images acquired on the second day flight session were used to this analysis. Four GCP distributions were examined using 12 GCPs for both image sets. All GCP distributions are illustrated in Figure 4.3. Check points were used to calculate geometric accuracy in each option and all the accuracies are shown in Table 4.3.

Only horizontal accuracy was considered in this section while vertical accuracy was neglected due to the unavailability of the bench mark height. According to the analysis, there is no significant accuracy change with the different number of GCPs and the different GCP distributions in RGB image model. The average RMSE for the RGB image model in all GCP options is 4.7 cm. Nevertheless, the RedEdge image model geometric accuracy would be affected by different GCP distribution. The highest accuracy was recorded from the GCP option P4 which gave 4.1 cm RMSE value. The P4 option used the highest number of GCPs as control points.

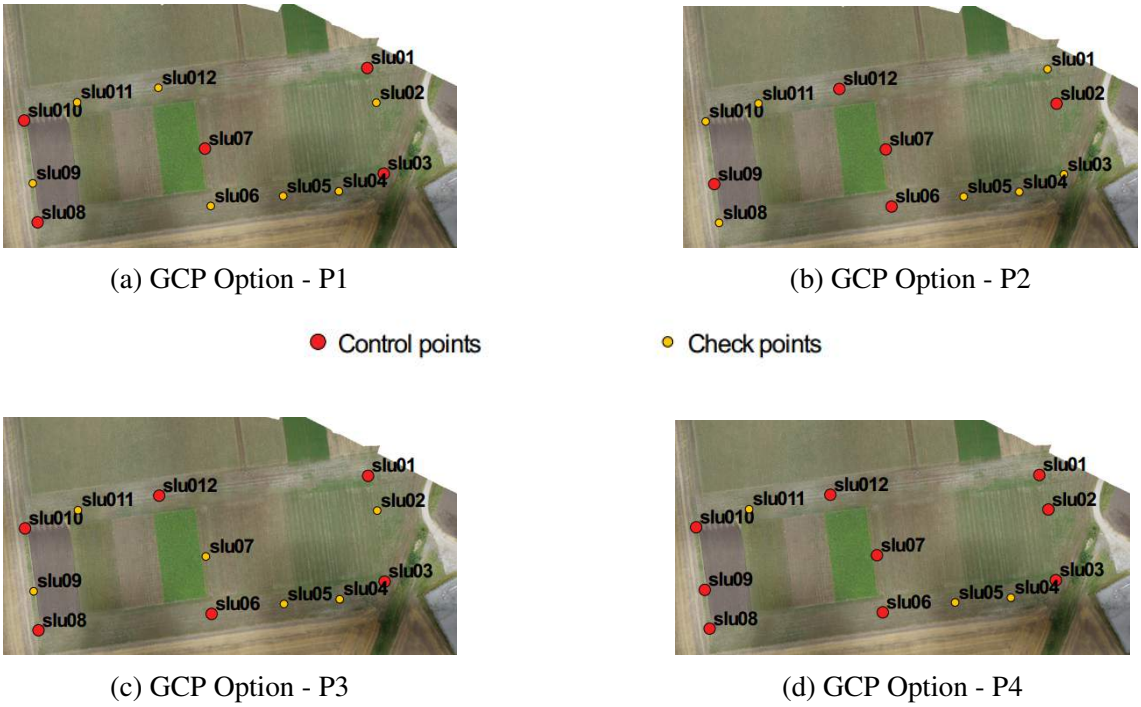


(a) GCP Option - P1

(b) GCP Option - P2

(c) GCP Option - P3

(d) GCP Option - P4

Figure 4.3: GCP distribution for geo-referencing

The configured GSD of the RGB image was 2 cm in the image acquisition and the obtained spatial resolution of the RGB ortho-mosaic was 2.1 cm. However, the geometric error of the mosaic was always more than two pixels. On the contrary, the mosaic from

RedEdge images lowest RMSE was less than a pixel in relation to the mosaic's resolution which was 5.6 cm. Later, the highest geometric quality processing was used to generate the DEM and ortho-mosaic from both image sets.

Table 4.3: GCP distributions and RMSE values

| Image Set | Option | $X_{RMSE}$ (cm) | $Y_{RMSE}$ (cm) | $XY_{RMSE}$ (cm) | $Z_{RMSE}$ (m) |
|---|---|---|---|---|---|
| RGB | P1 | 2.768 | 3.823 | 4.720 ± 2.045 | 15.196 |
| | P2 | 2.897 | 3.712 | 4.708 ± 1.742 | 30.890 |
| | P3 | 3.126 | 3.711 | 4.852 ± 2.087 | 17.033 |
| | P4 | 3.380 | 3.264 | 4.699 ± 3.113 | 1.245 |
| RedEdge | P1 | 3.408 | 6.219 | 7.091 ± 2.902 | 18.765 |
| | P2 | 4.090 | 4.386 | 5.997 ± 2.742 | 20.950 |
| | P3 | 3.929 | 6.385 | 7.497 ± 3.003 | 21.868 |
| | P4 | 3.459 | 2.174 | 4.085 ± 3.162 | 3.671 |

## 4.5 Digital Surface Models (DSM)

UAV image processing with the SFM method needs an overlapingimage set. The output quality of the product is increased with the number of overlap images. The overlap coverage maps for the both image sets are illustrated in Figure 4.4

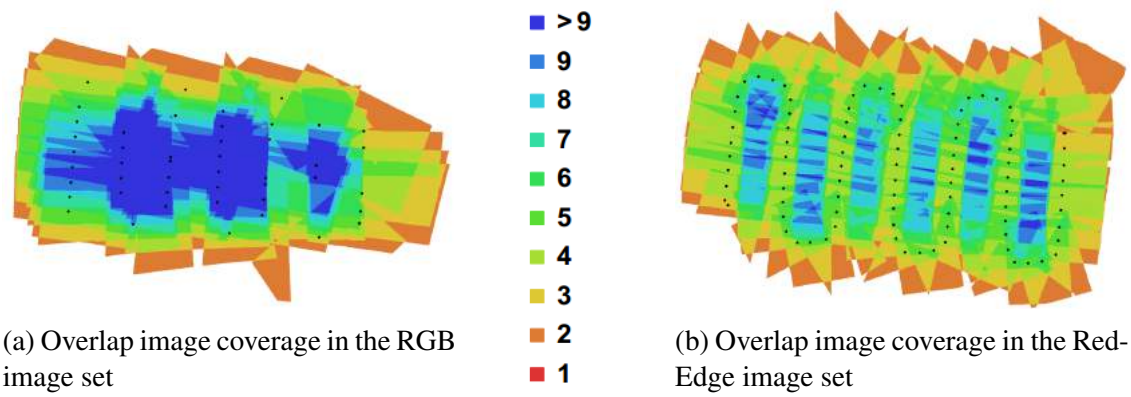


(a) Overlap image coverage in the RGB image set

(b) Overlap image coverage in the RedEdge image set

Figure 4.4: The UAV flight path and PSIQ values from the images

The DSM is one of the important products from the UAV RS. The RGB image set generated a DSM whose resolution was 4.2 cm per pixel. The DSM had 572 points per square-meter. In like manner, the second DSM was generated using the RedEdge image set. That DSM's resolution was 22.6 cm per pixel and its point density was 19.6 points per square-meter. The two DSMs from the both image sets are shown in Figure 4.5 and Figure 4.6.

Crop and tree pattern can be seen visually in the both DSMs. Hence, Elevation values over different features in the study area were evaluated to check the elevation differences.

Random points over crop area (barley), non-crop area and trees were extracted from both DSMs and compared. The extracted elevation values are presented in Figure 4.10 and Table 4.4. According to the elevation values, average elevation over the trees are 19.17 m and 19.67 m from the RGB DSM and the RedEdge DSM respectively. The average elevation difference between crop area and non-crop area was 0.27 m from the RGB DSM while it was 0.14 m in the RedEdge DSM. Based on this, it is confirmed that the DSMs are logically coherent qualitatively with the ground data.

Table 4.4: Elevation analysis values from DSMs

| Class | RGB DSM (m) | RE DSM (m) |
|---|---|---|
| Crop area | 15.25 ± 0.67 | 15.32 ± 0.61 |
| Non-crop area | 14.98 ± 0.57 | 15.18 ± 0.66 |
| Trees | 19.17 ± 2.51 | 19.67 ± 2.26 |

## 4.6 Ortho-rectified Image Mosaics

The final product form the UAV acquired images is an ortho-mosaic which can be used to generate value added products for PA applications. The ortho-mosaic is a mosaic created by using ortho-rectified UAV-borne images. It is the ultimate output from the PhotoScan processing. The ortho-mosaic generated using the RGB images had 2.1 cm/pix that was close to the original UAV image's resolution which is 2 cm/pix. 57488 tie points from the image set were used to create the RGB point cloud. The RGB ortho-mosaic contained 4 bands, 3 for Red, Blue and Green bands while the last one is an alpha band which is working as a transparency band. The RGB ortho-mosaic is shown in Figure 4.7.

An ortho-mosaic from the RedEdge image set was created using the optimal geometric model. The ortho-mosaic's spatial resolution was 5.6 cm/pix. It consisted of six image bands, the first five of them represent each spectral band of the RedEdge camera. A false colour composite (R = NIR, G = Red, B = Green) RedEdge image based ortho-mosaic is shown in Figure 4.8.

The up-to-date very high resolution products from the UAV RS can be used for further processing in the PA application. Torres-Sánchez *et al.* (2013) classified a UAV-borne image mosaic using an object based image classification technique to identify early season weeds over the farm area. Moreover, Candiago *et al.* (2015) have analysed Vegetation Indexes (VI) derived from UAV RS images for the PA application over vineyards and tomatoes. Following the aforementioned studies, Normalised Vegetation Different Index (NDVI) was derived using the multispectral image mosaic in this study and it is shown in Figure 4.9. The derived NDVI product values were not accurate quantitatively due to

uncalibrated DN values, but it provided qualitative information to identify crop area, non crop area of the study area. Similarly, the obtained product form UAV RS can be further processed according to PA applications.

## 4.7 Identified Issues

Blurry UAV-borne images cause to blurry areas in the ortho-mosaic. Three reasons were assumed as sources for the UAV image blurriness. They are UAV instability, wind and cloud shadow. The blurry spots were located and identified from both mosaics according to the sources and they are illustrated in Figure 4.11.

However, changing the blending mode parameter in the ortho-mosaic generation step in the PhotoScan reduced the blur effect in the outputs. Three options are available for the blending mode which are 1) mosaic, 2) average, and 3) disable. According to the outputs from the three methods, the average blending mode provided a less blurry mosaic but it showed the boundaries of the seam-line in comparison to the mosaic blending mode. The Figure 4.12 shows the results from the different blending modes.

The size and the pattern of the GCPs were good enough for identifying them on the the RGB camera images. However, the size of the GCP was not enough to be clearly identified from the RedEdge camera images. The Figure 4.13 shows how the GCP are visualised in each camera image in the maximum zoom. Not only the size of the GCP, but image blurriness and image saturation also affected the GCP identification from the photos.

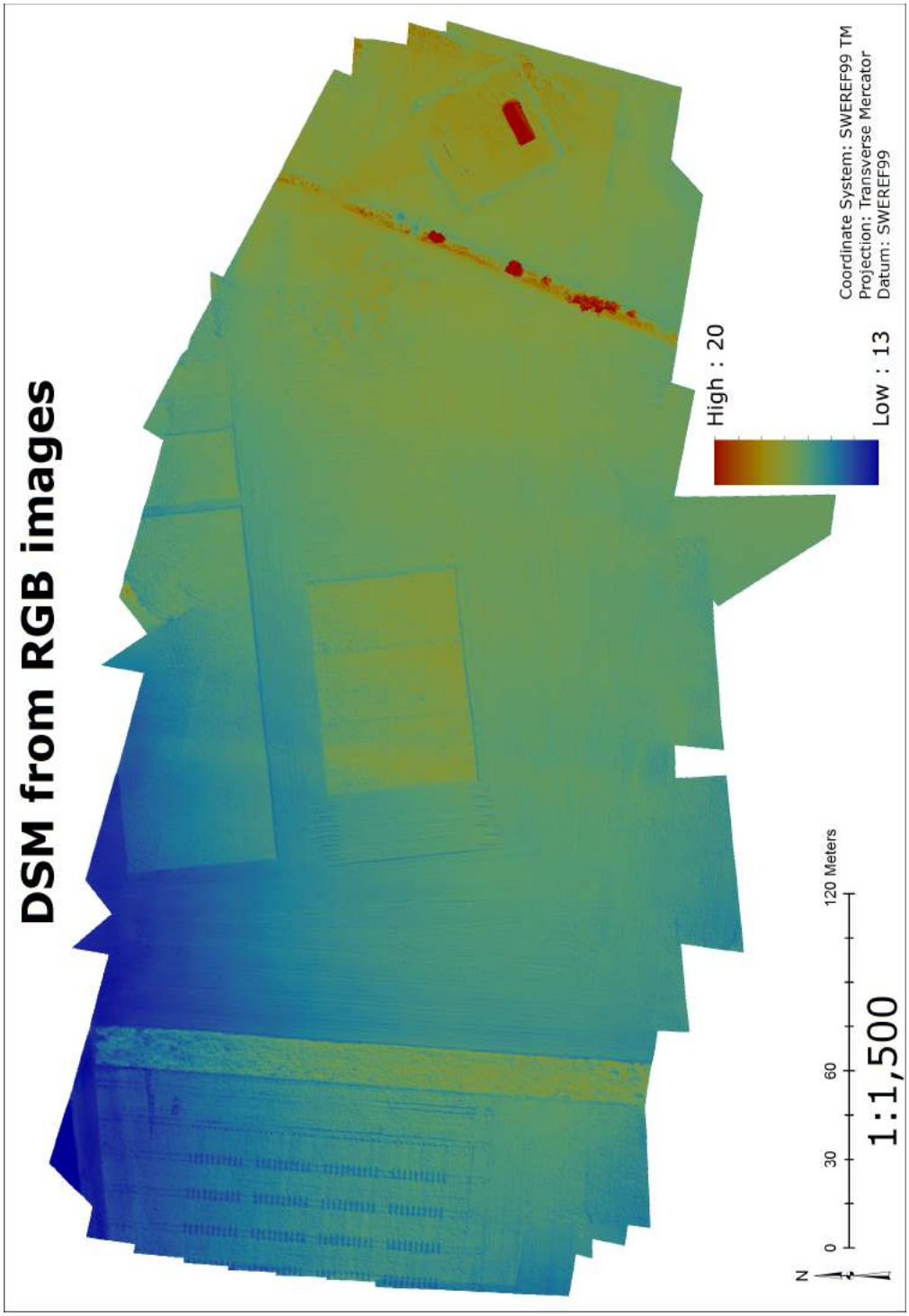


Figure 4.5: The DEM from the RGB image set

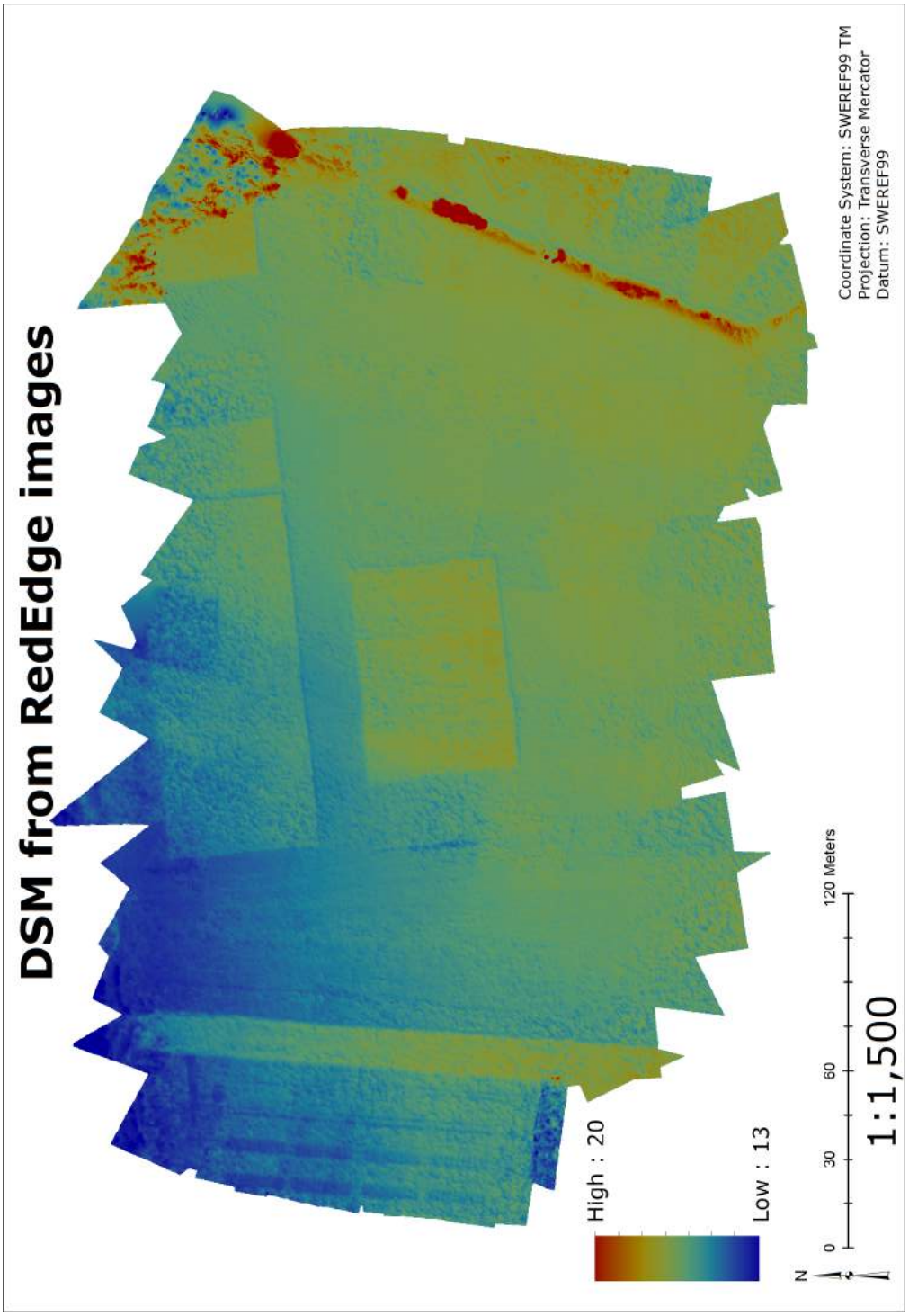


Figure 4.6: The DEM from the RedEdge image set

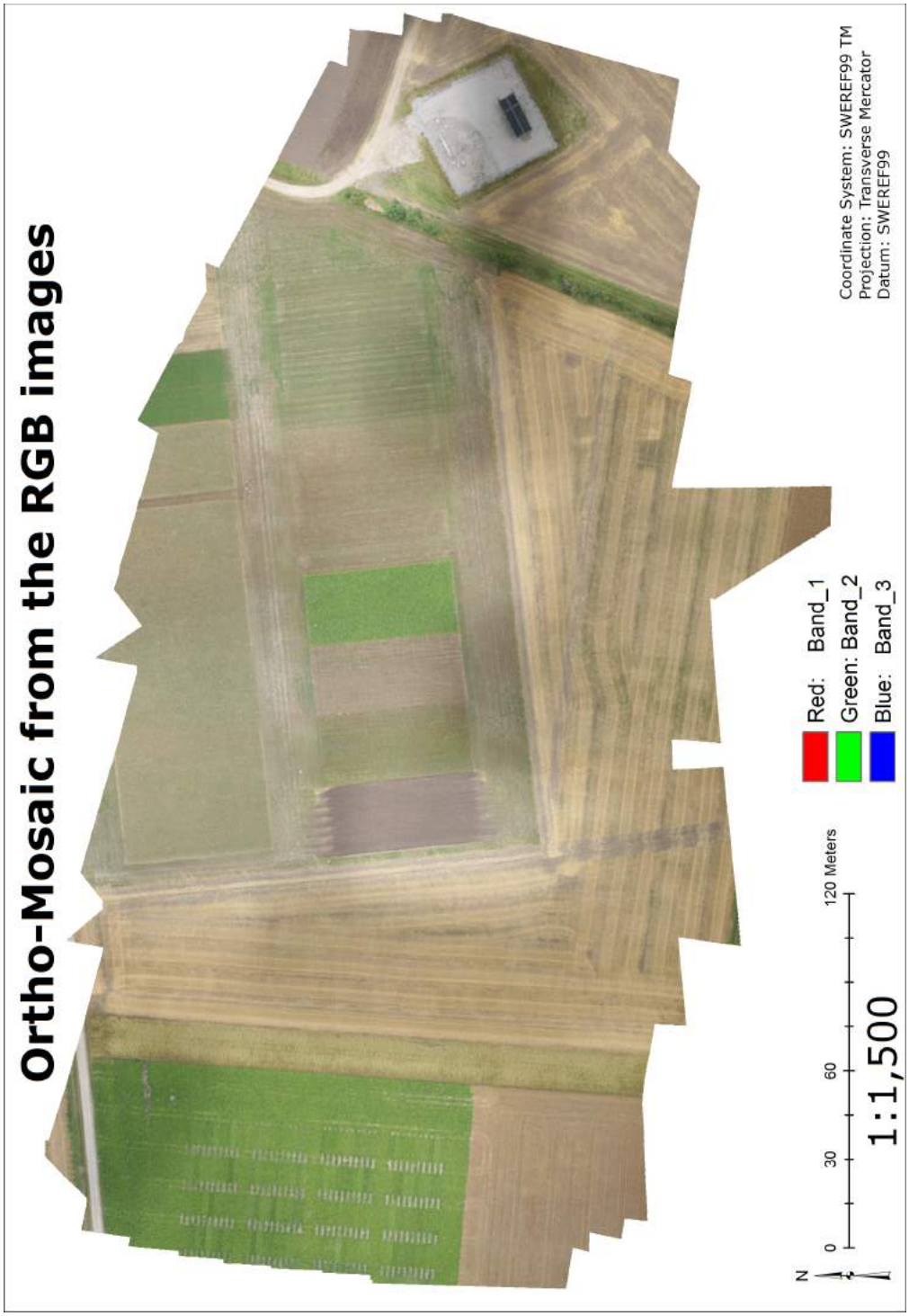


Figure 4.7: The ortho-mosaic generated from the RGB image set

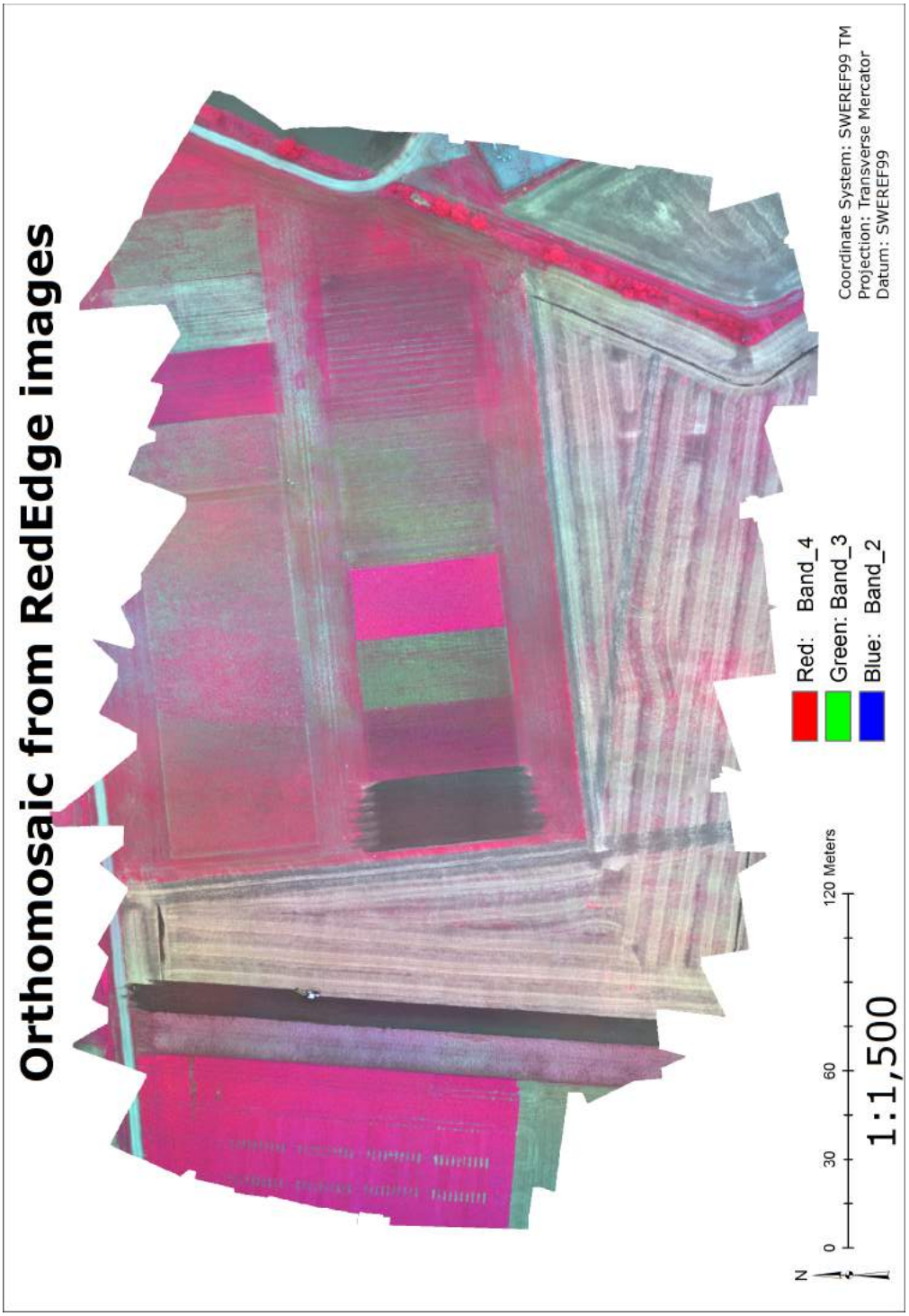


Figure 4.8: The ortho-mosaic generated from the RedEdge image set

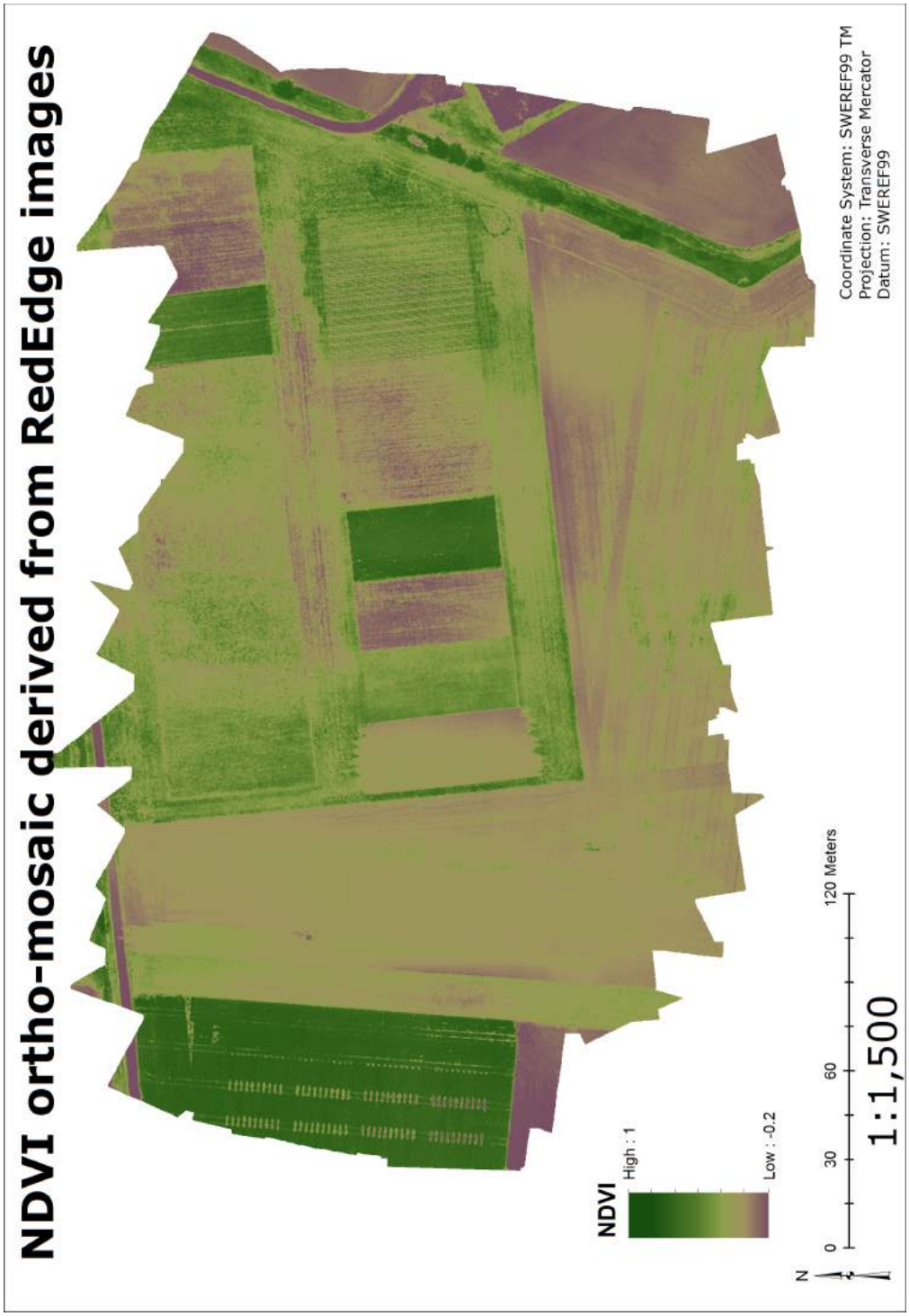


Figure 4.9: The NDVI mosaic image derived from the RedEdge ortho-mosaic

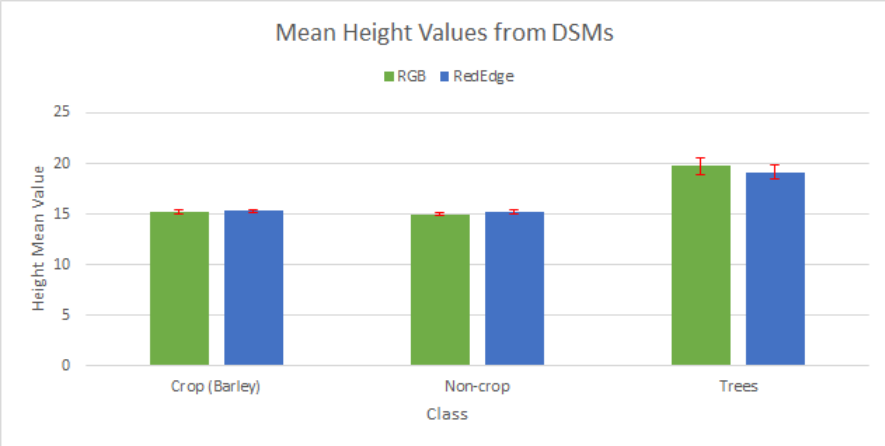


Figure 4.10: Mean height difference between from two DSMs

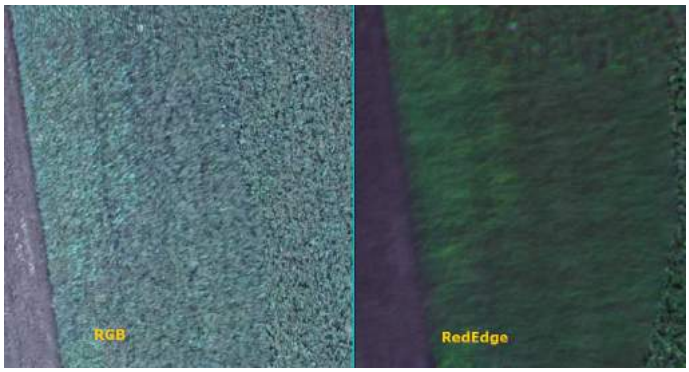


(a) Due to the UAV instability

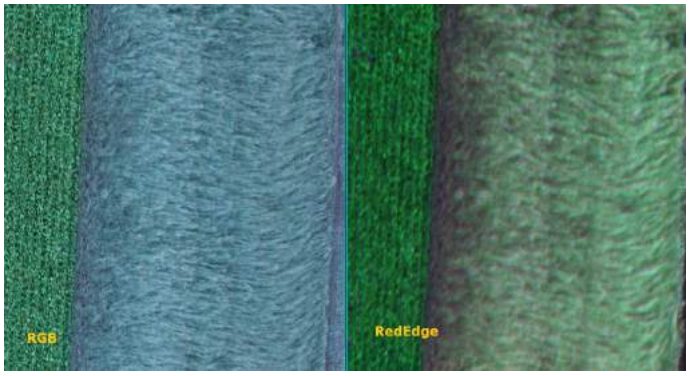


(b) Due to the shaking crops

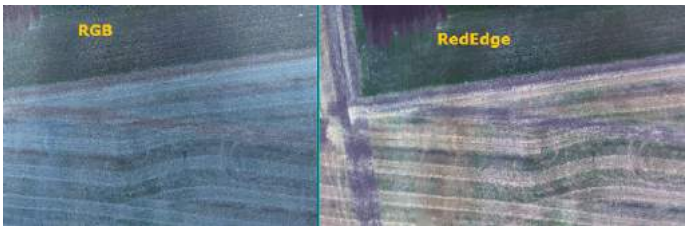


(c) Due to the cloud shadow

Figure 4.11: Identified blurry spots from the both image mosaics

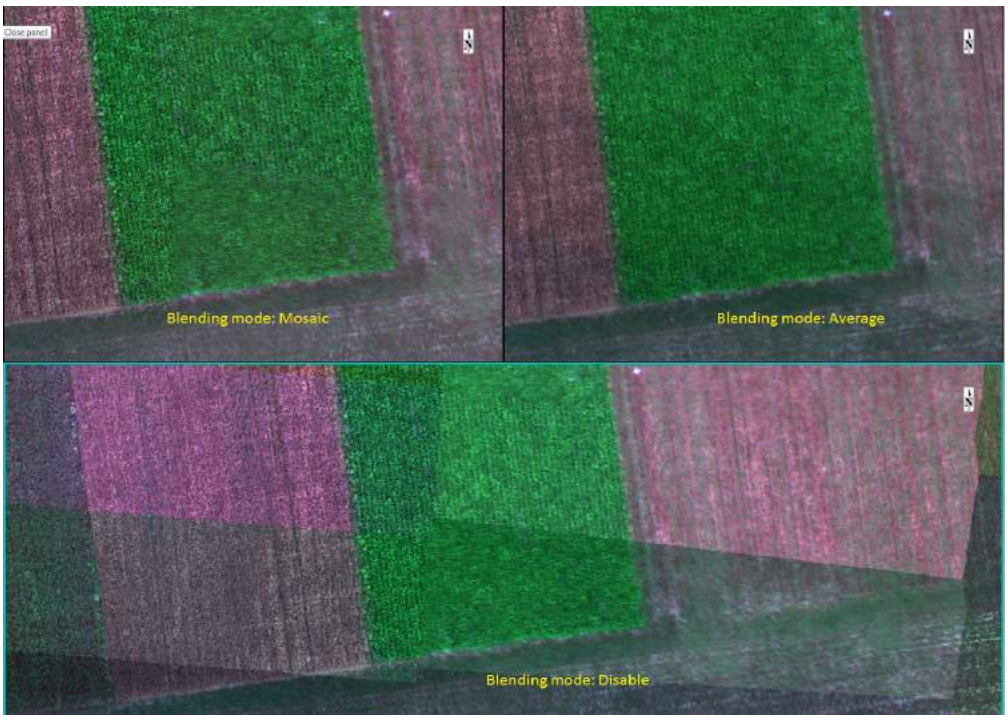


Figure 4.12: The effect of blending mode to the RedEdge mosaic

(a) The GCP in the RGB image

(b) The GCP in the RedEdge

(c) The GCP in the blurry RGB image

(d) The GCP in the blurry RedEdge

Figure 4.13: The GCP in different camera images

# Chapter 5

# Discussion

The multi-rotor UAV with two cameras was used to assess practical usage and to identify optimum configuration for the PA applications demonstrated in this study. The total sequential work procedure of the UAV RS using this Explorian UAV was identified in order to conduct the PA application. The work procedure include, battery charging, flight planing, the UAV flying and the UAV-borne image processing.

However, the study was constrained by limited availability of the UAV and the weather. The UAV was delayed to deliver by the manufacturer and it was repaired in the between the research work due to a power failure. Also, the thermal camera was malfunctioned during data collection. Furthermore, rain and wind held up the several flight missions that has been planned. Thus, only two flight session could be performed with in the limited time.

Ortho-rectified image mosaics from two different sensors and DSMs were derived using UAV-borne optical and multispectral camera images as the output RS products from this study. The spatial resolutions of the derived mosaics were significantly higher than both satellite and air-borne RS product. The RS product with few centimetre spatial resolution is ideal for the PA applications such as weed management (Torres-Sánchez *et al.* 2013), crop plant health monitoring, crop water stress monitoring, etc. Additionally, the UAV data collection can be deployed any stage of the farming provides an opportunity to obtain timely information for the PA applications.

The flying height is an important factor of the UAV RS especially in the PA applications. It is dependent with crop type and terrain undulation. In this study, UAV images covered several crop fields. Constant flying height was used due to lessen height variation of the crops and flat terrain. However, the Explorian UAV has an advantage of getting two different resolution products from two different cameras. Hence the constant flying height provides RS products with different resolution. Additionally, the flying height influences to the area of the mapping. In this study, GSD was configured to 2 cm for the

RGB camera then the flying height was derived from the GSD. Based on the RGB camera flying height the RedEdge camera height was configured. Consequently, the RGB camera provided 2.1 cm resolution product and the multispectral camera gave 5.6 cm resolution products. Computing the flying height from the required GSD and allows for the optimum flying height for the PA application.

The area of the mapping is a considerable parameter in the UAV RS. It is highly dependent with the flying time and the battery life time of the UAV. The Explorian UAV mentioned battery life (24 V) is about 25 minutes. Conversely, for a safety flying procedure the user is not allowed to utilise more than 50% (less than 22.1 V) battery life per one flight session. Therefore the maximum flying time of the UAV was 10-12 minutes. Accordingly, the area to be mapped was restricted with the flight time and a larger area was mapped using two separate batteries in two flight sessions with same flight configurations.

The flight planning estimated how many images will be taken in the flight session from the RGB camera. However, RGB images acquired from each flight session were notably less than the estimated value. Lesser number of images reduced the number overlap of the mapping area. The camera was triggered based on the distance travelled by the UAV. For that, distance was obtained using the UAV GPS reading. The inaccurate GPS readings affect the distance calculation and results to fail the camera triggering. Therefore, both distance and time should be used to trigger the camera and it is demonstrated from this study.

UAV image overlap percentage were recommended in several PA studies (Matese *et al.* 2015; Candiago *et al.* 2015). Hence, overlap percentage was not tested in this study and overlap percentages were defined based on the previous studies. It shows that 80% forward, 60% side overlaps for the RGB camera and 80% for both overlap for the RedEdge camera provided sufficient overlap coverage to perform SFM methodology. Images with higher overlap percentage can be matched accurately comparing to less overlap percentage image set. The RGB image data set showed that it covered most of the study area with more than 7 overlap images. In comparison, sides of the flight line areas were covered by more than 7 RedEdge images and the flight line area was covered by averagely less than 5 overlap images.

The UAV RS can overcome the problems in the satellite RS such as cloud cover and limited resolution. Nevertheless, the significant problem that was identified in the UAV RS is the blur effect of UAV RS products. The exact cause for the image blurriness could not be identified. However, it is assumed to be related due to the UAV instability, wind and cloud shadow. In this study, a gimbal was used for the RGB camera to reduce the motion effect of the UAV to the camera. However, the RedEdge camera was attached without a gimbal to the UAV. Therefore images from RGB camera were sharper than the

RedEdge camera due to the UAV movements. The wind also affected to the blurriness in the images in two ways. First, the wind can change the UAV stability and it can lead to increased image blurriness. On the other hand, crops like cereals (barley, wheat), can shake with the wind effects the images. Thus, same plants in different view angles will give different shapes and it can cause errors in the image matching in the UAV image processing. The cloud shadows also affect the image sharpness. The area covered by cloud shadow has a different light condition in comparison to the other area. Different light conditions will provide lesser quality images and it will reduce the final quality of the RS product. Although, the PhotoScan based image quality measurements (PSIQ) were used in this study to identify the non-focused, blurry images and to process only sharp images the results showed that, eliminating images based on PSIQ is not enough to enhance the output quality of the UAV RS. It has been noticed that blurriness of the input image affects to the final ortho-mosaic. The effect of the UAV-borne image blurriness can reduce the accuracy of the PA application even though it provides high resolution, timely information.

The geo-referenced UAV products can be obtained only using geo-tagged data from the UAV-borne images. However, the geometric accuracy of the products only using geo-tag information are not enough especially for the PA applications. In this study, external GCPs were used to geo-reference and to calculate geometric error of the products. Paper based printed temporary GCP were applied in this study. The size of the GCP must be increased proportionally to the GSD of both images and is one of the recommendations of this study. Every time the UAV was flown, GNSS observation was performed with temporary GCP locations.

According to the geometric analysis results, there is no significant relationship between the number of GCPs and the pattern of GCPs distribution and the geometric accuracy of the output. A minimum of well distributed 10 GCPs are enough to obtain required geometric accuracy over the similar size of agricultural plots. Usage of many GCPs provides the opportunity to select clearly visible GCPs for the geo-referencing. The absolute vertical error in the geo-referencing model was significantly higher due to unavailability of the vertical shift between two height reference system of the GCPs and images. It resulted in the absolute elevation accuracy in the derived DSM from UAV RS. However, it does not affect the relative elevation differences in the DSM. According to the elevation variation between crop area, tree area and non-crop area from the both DSM values proved that the DSM from the Explorian UAV can be applied for the PA application like crop growth monitoring, irrigation planing.

The UAV flight session was affected by the weather and the logistics. A few flight session were cancelled in this study period, due to the rain and the wind. Similarly, at least

three people (a pilot, a telemetry data observer, a UgCS software controller) preferred to be needed to perform the UAV flight session and several batteries (the UAV batteries, the RGB camera battery, the flight controller battery, the telemetry data viewer battery, etc,.) have to be charged before hand.

According to the literature, the optimum UAV RS product specification and quality criteria for the PA applications are dependent with the application type. The final products derived from the Explorian UAV has 2.1 cm and 5.6 cm spatial resolution and maximum two pixel and one pixel level geometric quality from both cameras respectively. The both products exceeded the given data specifications and quality criteria in the different application which were mentioned in the literature. Thus, this study demonstrated that the Explorian UAV is a potential platform for the PA applications. The two sensors which are attached to the UAV provide very high spatial resolution RS products that open many doors for the PA applications. Monitoring agriculture crop lands is essential to be done in correct time and the RS with the Explorian UAV showed it can be flown and collect and processed data timely. Additionally, advantages as well as drawbacks of the UAV RS for the PA applications were identified in this study. However to get accurate and precise results from the application the given recommendations and suggestions should be followed.

This study can be considered as a preliminarily study with the Explorian UAV for the PA applications due to limited resources and the time. However, to get full understanding of the optimum configuration of the UAV RS for the PA application few more test flights are recommended. Check for the UAV speed, test for the RGB camera triggering mode, Radiometric normalisation of the RedEdge camera, and identify image blurriness using different algorithm are some of the test that can be done in future based on this study.

# Chapter 6

# Conclusions

As a preliminary study with the Explorian UAV, this research work identified the optimum configurations to acquire images using the optical and the multispectral camera. The work-flow from the flight planning to the processing UAV-borne image data were proposed for the effective PA applications. The flying parameters to obtain very high resolution RS products for the PA applications (5 $ms^{-1}$ flying speed, 2 cm GSD, 80% forward overlap, 60% side overlap) were extracted from this study. The UAV-borne optical RGB camera and multispectral camera image processing with the SFM method using the Agisoft PhotoScan software was described in this thesis work. A 2.1 cm spatial resolution ortho-mosaic was generated from the optical RGB camera while the derived orhto-mosaic from the multispectral camera was 5.6 cm. Two different spectral and spatial resolution RS products can be obtained from the Explorian UAV using one flight session and with same flying height.

The UAV RS products quality was evaluated visually as well as geometrically. Visual evaluation indicated there is blur effect of the output and the UAV instability, wind, and cloud cover were noted as potential reasons for that. The blur effect of the images was quantified using the PhotoScan image quality measurement. Nevertheless it was not enough to track the blur effects of the input images. The geometric assessment of the UAV RS products showed, that the RGB image products can obtain a two pixel value geometric accuracy while the RedEdge camera product can get less than a pixel geometric accuracy using well distributed GCPs. The distribution of the GCPs and number of GCPs did not significantly affect the geometric accuracy of the product. A total of six well distributed GCPs are enough to get the required geometric quality over the area which has a size 0.07 $km^2$ flat area.

In conclusion, the UAV RS for the PA application is constantly evolving. Usage of the particular UAV with different sensors for the potential PA application was reported and limitations of the process was noted in this research work.

# Bibliography


1. Agisoft LLC. *Agisoft Photoscan User Manual - 1.2* tech. rep. (Agisoft LLC, 2016).
2. Candiago, S., Remondino, F., Giglio, M. D., Dubbini, M. & Gattelli, M. Evaluating Multispectral Images and Vegetation Indices for Precision Farming Applications from UAV Images. *Remote Sensing* **7,** 4026–4047 (2015).
3. Colomina, I. & Molina, P. Unmanned aerial systems for photogrammetry and remote sensing: A review. *ISPRS Journal of Photogrammetry and Remote Sensing* **92,** 79–97 (2014).
4. Dandois, J., Marc, O. & Erle, E. Optimal Altitude, Overlap, and Weather Conditions for Computer Vision UAV Estimates of Forest Structure. *Remote Sensing* **7,** 13895–13920 (2015).
5. Del Pozo, S., Rodríguez-Gonzálvez, P., Hernández-López, D. & Felipe-García, B. Vicarious Radiometric Calibration of a Multispectral Camera on Board an Unmanned Aerial System. *Remote Sensing* **6,** 1918–1937 (2014).
6. DJI-Innovations. *Ground Station Wireless Data-link User Manual - Version 3.04* tech. rep. (DJI Innovations, 2015).
7. Eisenbeiss, H. *UAV Photogrammetry* PhD thesis (2009), 201.
8. Everaerts, J. in *Advances in Photogrammetry, Remote Sensing and Spatial Information Sciences* 117–124 (CRC Press, Taylor & Francis Group, London, 2008).
9. Furukawa, Y. & Ponce, J. Accurate, Dense, and Robust Multi-View Stereopsis. *IEEE Trans. on Pattern Analysis and Machine Intelligence* **32,** 1362–137 (2010).
10. Goldstein, E. B., Oliver, A. R., Moore, L. J., Jass, T., *et al. Ground control point requirements for structure-from-motion derived topography in low-slope coastal environments* tech. rep. (PeerJ PrePrints, 2015).
11. Greenwood, F. in *Drones and aerial observation: New technologies for property rights, human rights, and global development* 35–47 (New America, 2015).

12. Gross, J. W. *A Comparison of Orthomosaic Software for Use with Ultra High Resolution Imagery of a Wetland Environment* in *Proceedings of the IMAGIN Student Poster & Paper Competition, 2015* Traverse City, June 8, 2015 (Improving Michigan's Access to Geographic Information Network - IMAGIN, 2015).

13. Jedlika, K. Accuracy of Surface Models Acquired from Different Sources — Important Information for Geomorphological Research. *Geomorphologia Slovaca Et Bohemica,* 17–28 (2009).

14. Kedzierski, M. & Wierzbicki, D. Radiometric quality assessment of images acquired by UAV's in various lighting and weather conditions. *Measurement* **76,** 156–169 (2015).

15. Laliberte, A. S., Herrick, J. E., Rango, A. & Winters, C. Acquisition , Or thorectification , and Object-based Classification of Unmanned Aerial Vehicle (UAV) Imagery for Rangeland Monitoring. *Photogrammetric Engineering Remote Sensing* **76,** 661–672 (2010).

16. L'hotellier, E. *Height Altitude Flight level* tech. rep. September (IVAO HQ training department, 2015), 1–5.

17. Ma, L., Li, M., Tong, L., Wang, Y. & Cheng, L. Using unmanned aerial vehicle for remote sensing application. *2013 21st International Conference on Geoinformatics,* 1–5 (2013).

18. Matese, A. *et al.* Intercomparison of UAV, Aircraft and Satellite Remote Sensing Platforms for Precision Viticulture. *Remote Sensing* **7,** 2971–2990 (2015).

19. Mathews, A. A practical UAV remote sensing methodology to generate multispectral orthophotos for vineyards: estimation of spectral reflectance using compact digital cameras. *International Journal of Applied Geospatial Research (IJAGR)* **6,** 65–87 (2015).

20. Mesas-Carrascosa, F. J., Rumbao, I. C., Berrocal, J. A. B. & Porras, A. G. F. Positional quality assessment of orthophotos obtained from sensors onboard multi-rotor UAV platforms. *Sensors (Switzerland)* **14,** 22394–22407 (2014).

21. Micasense. *MicaSense RedEdge TM 3 Multispectral Camera User Manual* tech. rep. May (2015), 1–27.

22. Nesbit, P. R. *Uninhabited Aerial Vehicles and Structure From Motion : A fresh approach to photogrammetry* Dissertation (California State University, Long Beach, 2014), 177.

23. Nissen, E., Johnson, K., Fitzgerald, F., Morgan, M. & White, J. Rapid-Response or Repeat-Mode Topography from Aerial Structure from Motion. *AGU Fall Meeting Abstracts* (2014).

24. Pasumansky, A. *Estimate image quality* 2014. <http://www.agisoft.com/forum/index.php?topic=2179.0> (visited on 08/06/2016).

25. Pix4D. *Pix4D Introduction Guide* tech. rep. October (Pix4D, 2013).

26. Primicerio, J., Di Gennaro, S. F., Fiorillo, E., Genesio, L., Lugato, E., Matese, A. & Vaccari, F. P. A flexible unmanned aerial vehicle for precision agriculture. *Precision Agriculture* **13,** 517–523 (2012).

27. Riazanoff, S. & Santer, R. in *Fundamentals of Spatial Data Quality* (eds Devillers, R. & Jeansoulin, R.) 61–87 (ISTE, 2006).

28. Rosebrock, A. *Blur detection with OpenCV* 2015. <http://www.pyimagesearch.com/2015/09/07/blur-detection-with-opencv/> (visited on 05/02/2016).

29. Salamı, E., Barrado, C. & Pastor, E. UAV Flight Experiments Applied to the Remote Sensing of Vegetated Areas. *Remote Sensing* **6,** 11051–11081 (2014).

30. Semyonov, D. *Algorithms used in Photoscan* 2011. <http://www.agisoft.com/forum/index.php?topic=89.0> (visited on 02/01/2016).

31. Snavely, N. *Scene Reconstruction and Visualization from Internet Photo Collections: A Survey* PhD thesis (2011), 44–66.

32. Sony. *Interchangeable Lens Digital Camera NEX-7* tech. rep. 1 (2011), 64.

33. Tang, L. & Shao, G. Drone remote sensing for forestry research and practices. *Journal of Forestry Research* **26,** 1–7 (2015).

34. The Weather Company, L. *Weather Underground* <https://www.wunderground.com/history/airport/ESMS/2016/08/22/DailyHistory.html?req_city=Lund&req_statename=Sweden&reqdb.zip=00000&reqdb.magic=6&reqdb.wmo=02627> (2016).

35. Torres-Sánchez, J., López-Granados, F., De Castro, A. I. & Peña-Barragán, J. M. Configuration and Specifications of an Unmanned Aerial Vehicle (UAV) for Early Site Specific Weed Management. *PLoS ONE* **8,** 1–15 (2013).

36. Wei, Y.-M., Kang, L., Yang, B. & Wu, L.-D. Applications of structure from motion: a survey *. *J Zhejiang Univ-Sci C (Comput & Electron) Journal of Zhejiang University-SCIENCE C (Computers & Electronics* **14,** 486–494 (2013).

37. Westoby, M. J., Brasington, J., Glasser, N. F., Hambrey, M. J. & Reynolds, J. M. 'Structure-from-Motion' photogrammetry: A low-cost, effective tool for geoscience applications. *Geomorphology* **179,** 300–314 (2012).

38. Xie, Y., Sha, Z. & Yui, M. Remote sensing imagery in vegetation mapping: a review. *Journal of Plant Ecology-Uk* **1,** 9–23 (2008).

39. Yudi, S., Muhammad, I. L., Lilik, B. P., Iskandar, Z. S., Hefni, E. & Catur, A. R. The 1st International Symposium on LAPAN-IPB Satellite (LISAT) for Food Security and Environmental Monitoring The Potential of UAV-based Remote Sensing for Supporting Precision Agriculture in Indonesia. *Procedia Environmental Sciences* **24,** 245–253 (2015).

40. Zhang, C. & Kovacs, J. M. The application of small unmanned aerial systems for precision agriculture: a review. *Precision Agriculture* **13,** 693–712 (2012).

**Institutionen för naturgeografi och ekosystemvetenskap, Lunds Universitet.**

Student examensarbete (Seminarieuppsatser). Uppsatserna finns tillgängliga på institutionens geobibliotek, Sölvegatan 12, 223 62 LUND. Serien startade 1985. Hela listan och själva uppsatserna är även tillgängliga på LUP student papers (`https://lup.lub.lu.se/student-papers/search/`) och via Geobiblioteket (`http://www.geobib.lu.se/`)

The student thesis reports are available at the Geo-Library, Department of Physical Geography and Ecosystem Science, University of Lund, Sölvegatan 12, S-223 62 Lund, Sweden. Report series started 1985. The complete list and electronic versions are also electronic available at the LUP student papers (`https://lup.lub.lu.se/student-papers/search/`) and through the Geo-library (`http://www.geobib.lu.se/`)

350 Mihaela – Mariana Tudoran (2015) Occurrences of insect outbreaks in Sweden in relation to climatic parameters since 1850
351 Maria Gatzouras (2015) Assessment of trampling impact in Icelandic natural areas in experimental plots with focus on image analysis of digital photographs
352 Gustav Wallner (2015) Estimating and evaluating GPP in the Sahel using MSG/SEVIRI and MODIS satellite data
353 Luisa Teixeira (2015) Exploring the relationships between biodiversity and benthic habitat in the Primeiras and Segundas Protected Area, Mozambique
354 Iris Behrens & Linn Gardell (2015) Water quality in Apac-, Mbale- & Lira district, Uganda - A field study evaluating problems and suitable solutions
355 Viktoria Björklund (2015) Water quality in rivers affected by urbanization: A Case Study in Minas Gerais, Brazil
356 Tara Mellquist (2015) Hållbar dagvattenhantering i Stockholms stad - En riskhanteringsanalys med avseende på långsiktig hållbarhet av Stockholms stads & dagvattenhantering i urban miljö
357 Jenny Hansson (2015) Trafikrelaterade luftföroreningar vid förskolor – En studie om kvävedioxidhalter vid förskolor i Malmö
358 Laura Reinelt (2015) Modelling vegetation dynamics and carbon fluxes in a high Arctic mire

359 Emelie Linnéa Graham (2015) Atmospheric reactivity of cyclic ethers of relevance to biofuel combustion
360 Filippo Gualla (2015) Sun position and PV panels: a model to determine the best orientation
361 Joakim Lindberg (2015) Locating potential flood areas in an urban environment using remote sensing and GIS, case study Lund, Sweden
362 Georgios-Konstantinos Lagkas (2015) Analysis of NDVI variation and snowmelt around Zackenberg station, Greenland with comparison of ground data and remote sensing.
363 Carlos Arellano (2015) Production and Biodegradability of Dissolved Organic Carbon from Different Litter Sources
364 Sofia Valentin (2015) Do-It-Yourself Helium Balloon Aerial Photography - Developing a method in an agroforestry plantation, Lao PDR
365 Shirin Danehpash (2015) Evaluation of Standards and Techniques for Retrieval of Geospatial Raster Data - A study for the ICOS Carbon Portal
366 Linnea Jonsson (2015) Evaluation of pixel based and object based classification methods for land cover mapping with high spatial resolution satellite imagery, in the Amazonas, Brazil.
367 Johan Westin (2015) Quantification of a continuous-cover forest in Sweden using remote sensing techniques
368 Dahlia Mudzaffar Ali (2015) Quantifying Terrain Factor Using GIS Applications for & Real Estate Property Valuation
369 Ulrika Belsing (2015) The survival of moth larvae feeding on different plant species in northern Fennoscandia
370 Isabella Grönfeldt (2015) Snow and sea ice temperature profiles from satellite data and ice mass balance buoys
371 Karolina D. Pantazatou (2015) Issues of Geographic Context Variable Calculation Methods applied at different Geographic Levels in Spatial Historical Demographic Research -A case study over four parishes in Southern Sweden
372 Andreas Dahlbom (2016) The impact of permafrost degradation on methane fluxes - a field study in Abisko
373 Hanna Modin (2016) Higher temperatures increase nutrient availability in the High Arctic, causing elevated competitive pressure and a decline in Papaver radicatum
374 Elsa Lindevall (2016) Assessment of the relationship between the Photochemical Reflectance Index and Light Use Efficiency: A study of its seasonal and diurnal variation in a sub-arctic birch forest, Abisko, Sweden
375 Henrik Hagelin and Matthieu Cluzel (2016) Applying FARSITE and Prometheus on the Västmanland Fire, Sweden (2014): Fire Growth Simulation as a Measure Against Forest Fire Spread – A Model Suitability Study –
376 Pontus Cederholm (2016) Californian Drought: The Processes and Factors Controlling the 2011-2016 Drought and Winter Precipitation in California

377 Johannes Loer (2016) Modelling nitrogen balance in two Southern Swedish spruce plantations
378 Hanna Angel (2016) Water and carbon footprints of mining and producing Cu, Mg and Zn: A comparative study of primary and secondary sources
379 Gusten Brodin (2016) Organic farming's role in adaptation to and mitigation of climate change - an overview of ecological resilience and a model case study
380 Verånika Trollblad (2016) Odling av Cucumis Sativus L. med aska från träd som näringstillägg i ett urinbaserat hydroponiskt system
381 Susanne De Bourg (2016) Tillväxteffekter för andra generationens granskog efter tidigare genomförd kalkning
382 Katarina Crafoord (2016) Placering av energiskog i Sverige - en GIS analys
383 Simon Nåfält (2016) Assessing avalanche risk by terrain analysis An experimental GIS-approach to The Avalanche Terrain Exposure Scale (ATES)
384 Vide Hellgren (2016) Asteroid Mining - A Review of Methods and Aspects
385 Tina Truedsson (2016) Hur påverkar snömängd och vindförhållande vattentrycksmätningar vintertid i en sjö på västra Grönland?
386 Chloe Näslund (2016) Prompt Pediatric Care Pediatric patients' estimated travel times to surgically-equipped hospitals in Sweden's Scania County
387 Yufei Wei (2016) Developing a web-based system to visualize vegetation trends by a nonlinear regression algorithm
388 Greta Wistrand (2016) Investigating the potential of object-based image analysis to identify tree avenues in high resolution aerial imagery and lidar data
389 Jessica Ahlgren (2016) Development of a Web Mapping Application for grazing resource information in Kordofan, Sudan, by downloading MODIS data automatically via Python
390 Hanna Axén (2016) Methane flux measurements with low-cost solid state sensors in Kobbefjord, West Greenland
391 Ludvig Forslund (2016) Development of methods for flood analysis and response in a Web-GIS for disaster management
392 Shuzhi Dong (2016) Comparisons between different multi-criteria decision analysis techniques for disease susceptibility mapping
393 Thirze Hermans (2016) Modelling grain surplus/deficit in Cameroon for 2030
394 Stefanos Georganos (2016) Exploring the spatial relationship between NDVI and rainfall in the semi-arid Sahel using geographically weighted regression
395 Julia Kelly (2016) Physiological responses to drought in healthy and stressed trees: a comparison of four species in Oregon, USA
396 Antonín Kusbach (2016) Analysis of Arctic peak-season carbon flux estimations based on four MODIS vegetation products

397 Luana Andreea Simion (2016) Conservation assessments of Văcărești urban wetland in Bucharest (Romania): Land cover and climate changes from 2000 to 2015

398 Elsa Nordén (2016) Comparison between three landscape analysis tools to aid conservation efforts

399 Tudor Buhalău (2016) Detecting clear-cut deforestation using Landsat data: A time series analysis of remote sensing data in Covasna County, Romania between 2005 and 2015

400 Sofia Sjögren (2016) Effective methods for prediction and visualization of contaminated soil volumes in 3D with GIS

401 Jayan Wijesingha (2016) Geometric quality assessment of multi-rotor unmanned aerial vehicle-borne remote sensing products for precision agriculture